Materials Advances

ROYAL SOCIETY OF CHEMISTRY

REVIEW

View Article Online
View Journal

Check for updates

Cite this: DOI: 10.1039/d5ma00686d

Two-dimensional halide perovskite memristors for resistive switching memory systems

Hyojung Kim

Two-dimensional (2D) halide perovskites have surfaced as a dynamic platform for energy-efficient resistive switching memories. The atomic-scale slicing into Ruddlesden–Popper, Dion–Jacobson, vacancy-ordered, and single-crystal configurations allow for control over quantum confinement, ion transport, and interface energetics. This review looks into the latest advancements in the design, processing, and integration of devices for low-power memristors using 2D halide perovskite structures. The properties of solution-based spin coating and single-source vapor deposition are analyzed in terms of their effectiveness in producing vertically aligned grains, defect-passivated surfaces, and pinhole-free ultrathin films on both rigid and flexible substrates. The rectification and multilevel conductance, caused by built-in potential barriers and precise compliance control, enable selector-free crossbar arrays while reducing sneak current. Moreover, biologically inspired pulse procedures exhibit short-term dynamics and long-term potentiation, emphasizing the significant potential for neuromorphic devices. The insights gathered in this compilation offer actionable strategies for evolving 2D halide perovskites from their potential in the lab into dependable, multifunctional components for advanced memory and computing technologies.

Received 28th June 2025,
Accepted 1st October 2025

DOI: 10.1039/d5ma00686d

rsc.li/materials-advances

Open Access Article. Published on 03 octobre 2025. Downloaded on 2026-02-04 10:39:24.
This article is licensed under a Creative Commons Attribution 3.0 Unported Licence.

1. Introduction

The present information age has notably elevated standards for sophisticated hardware, especially regarding operational metrics and production quality.[1–10] Given the difficulties encountered by contemporary silicon-based architectures in meeting rising benchmarks, there is an increasing emphasis on novel active materials, especially metal-oxide semiconductors, organic semiconductors, and two-dimensional (2D) systems.[11–19] 2D halide perovskites offer quantum-well confinement, significant dielectric contrast, and extensive chemical adaptability, allowing for the precise engineering of their optical bandgaps, exciton dynamics, and lattice polarity.[20] Halide vacancies and mobile metal cations migrate under moderate electric fields, initiating electrochemical metallization or valence change that changes the resistance of a thin film while preserving its crystallinity. Halide-perovskite memristors exploit this behavior, operate at low bias, provide multilayer conductance, and preserve data for significant durations. When configured in passive crossbar arrays, they integrate logic and memory, avoiding the von Neumann bottleneck and allowing simultaneous analog vector–matrix multiplication.[21,22] Recent demonstrations of current rectification have significantly reduced sneak-path leakage and eliminated the need for external selectors in dense matrices.

In addition to these developments, recent investigations indicate that mixed-dimensional perfluoroarene perovskite heterostructures significantly improve device endurance in ambient environments, benzylammonium-based Ruddlesden–Popper layers provide consistent resistive switching with synaptic capabilities for neuromorphic computing, and blade-coated quasi-2D Pb–Sn memory devices enable scalable processing.[23–25]

However, performance depends on the manipulation of interface energetics, shape, and composition. Vertically aligned Ruddlesden–Popper layers reduce grain-boundary scattering, Dion–Jacobson phases enhance mechanical robustness, and vacancy-ordered bismuth- and antimony-based frameworks ensure lead-free stability.[26,27] Growth methods, including solvent-engineered spin coating and single-source vapor co-sublimation, have been developed to prevent uncontrolled nucleation, increase grain size, and provide pinhole-free coverage on both flexible and rigid substrates.

Scalable manufacturing relies on deposition methods that provide uniformity at wafer or web scale, precise control over stoichiometry, and vertical texture free of pinholes, all while adhering to low-temperature back-end-of-line constraints and lithographic patterning requirements. Solution processes need to control solvent-front dynamics, effectively dry gradients, and precursor rheology to reduce coffee-ringing and ensure uniform thickness. In contrast, vapor methods rely on a

Department of Semiconductor Systems Engineering, Sejong University, Seoul 05006, Korea. E-mail: hyojungkim0912@sejong.ac.kr

© 2026 The Author(s). Published by the Royal Society of Chemistry

Open Access Article. Published on 03 octobre 2025. Downloaded on 2026-02-04 10:39:24.
This article is licensed under a Creative Commons Attribution 3.0 Unported Licence.

balanced multi-zone flux and inline rate metrology to prevent phase segregation over extensive areas. The reproducibility at the array scale is influenced by variability between tools, the management of contamination, and the parameters of statistical process control. Factors that detract from yield can be attributed to particulate defects, interdiffusion between electrodes and perovskite, as well as failures in step coverage related to topography.

This review presents a thorough examination of design ideas for low-power resistive memories using 2D halide perovskites. We initially compare and analyze the electrical properties of multilayer and vacancy-ordered lattices, as well as Ruddlesden–Popper, Dion–Jacobson, and defect-ordered single crystals, to elucidate structure–function relationships. Subsequently, we elucidate how solution and vapor growth kinetics, in conjunction with electrode-interface engineering, influence filament stability and uniformity of switching. Device-level metrics, such as self-rectification, multilevel conductance, and mechanical durability on flexible substrates, are subsequently analyzed from a circuit perspective to evaluate their suitability for neuromorphic and high-density crossbar arrays. Ultimately, we define the prevailing obstacles and suggest research directions to expedite the practical implementation of these nascent electronic materials, thereby explaining the extent and importance of this effort.

A design map that considers various mechanisms has been developed, connecting the redox activity of electrodes, the energy required for halide-vacancy formation, and the anisotropy of the microstructure to key factors such as the primary switching mode, thresholds, rectification, and variability. Active Ag/Cu contacts combined with lattices that show low defect-formation energies and vertically aligned grains promote operation toward abrupt ECM with sub-volt SET, notable compliance dependence, and easily addressable multilevel states; inert electrodes paired with higher migration barriers and defect-suppressed single- or vacancy-ordered crystals support interface-limited VCM with wider yet more temperature-stable windows. Selector-free crossbars achieve optimal performance when inherent asymmetry provides robust rectification at the read bias, all while maintaining linearity in analog weight updates during pulse trains.

In contrast with conventional metal-oxide memristors, which depend on the movement of oxygen vacancies within stable lattices and demonstrate superior endurance and thermal capacity, 2D halide perovskites use flexible ionic structures and engineered anisotropy to achieve low-bias switching and effective built-in rectification. In comparison to organic polymer memories that provide printability and mechanical compliance yet frequently face limitations due to stochastic ionic transport and interfacial drift, layered halide perovskites enable enhanced compliance or pulse-programmed multilevel conductance, achieving better state separability through controlled crystallographic alignment. The methods of low-temperature solution and single-source vapor routes, along with vertical texturing, enable conformal integration on flexible substrates and passive crossbars, all while maintaining precise nanoscale thickness control and effective interface passivation

2. Layered halide perovskites for tunable optoelectronic functionality

Two-dimensional (2D) layered halide perovskites are composed of atomically thin inorganic layers arranged in a repetitive structural pattern, alternating with charge-balancing organic ions. This architecture supports a wide range of possibilities for optoelectronic and photonic devices. The transition from three-dimensional (3D) to 2D or quasi-2D morphologies often stems from spatial constraints encountered during the growth of ABX_3 crystals. This is particularly evident when long-chain aliphatic or aromatic ammonium ligands are included while maintaining the overall stoichiometry of ABX_3. The introduction of a substantial spacer cation, represented as $(A')_mA_{n-1}B_nX_{3n+1}$ $(1 \leq n \leq \infty)$,[30–32] leads to the development of distinctly separated layers in Fig. 1.[28] As n approaches infinity, the arrangement begins to focus on the traditional 3D perovskite structure, while $n = 1$ results in the thinnest monolayer equivalent.[33–35] Intermediate integer n values produce quasi-2D crystals that span the compositional continuum between these extremes. In these quasi-2D domains, significant quantum confinement is observed due to electronic multi-quantum wells, where inorganic BX_6 sheets function as "wells" and organic molecules serve as "barriers".[36,37] The significant dielectric disparity between these areas enhances Coulombic attraction, resulting in notably elevated exciton binding energies.

Crystallographically, the perovskite framework can be theoretically divided along the (100), (110), and (111) crystallographic axes in Fig. 2.[29,38] In the (100) orientation, planar inorganic slabs of thickness n are aligned along (100) about the parent lattice. The extensive compositional variability of the organic spacer allows significant chemical diversity, establishing this group as the most extensively examined subset

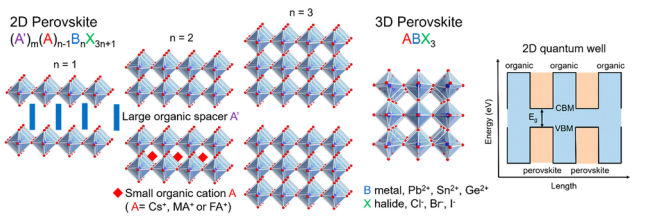

Fig. 1 Schematic representation of the transition from 2D perovskite to 3D perovskite, showing essential components and an illustration of the 2D quantum well structure. Reproduced with permission.[28] Copyright 2018, American Chemical Society.

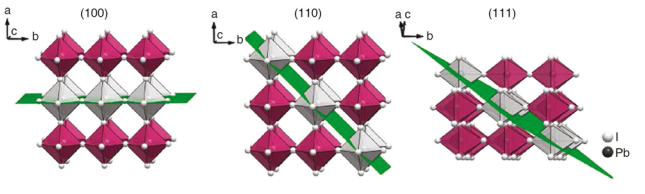

Fig. 2 Derivation of 2D halide perovskites from the parent cubic perovskite lattice of 3D layered halide perovskites by sectioning the latter along standard crystallographic planes: (100), (110), and (111). Reproduced from Han *et al.*,[29] licensed under CC BY 4.0.

© 2026 The Author(s). Published by the Royal Society of Chemistry

Open Access Article. Published on 03 octobre 2025. Downloaded on 2026-02-04 10:39:24. This article is licensed under a Creative Commons Attribution 3.0 Unported Licence.

of layered perovskites. In Ruddlesden–Popper architectures, a 3D ABX_3 network interacts with a 2D $(A')_2BX_4$ sheet to form $(A')_mA_{n-1}B_nX_{3n+1}$.[39–41] The R-NH_3 unit can include various alkyl or aryl ammonium cations. The Dion–Jacobson analogs, which are named after their oxide counterparts, exhibit a comparable topology. Nevertheless, the introduction of a divalent cation between the slabs removes lateral offsets, allowing the successive inorganic layers to align directly on top of one another. The complex species defined by $A_2A'_mB_mX_{3m+2}$ $(m > 1)$ are obtained from cleavage parallel to (110).[38,42] While there are encouraging developments, the number of effective light-harvesting layers reported is still limited. This is due to the ongoing challenges in achieving precise control over distorted slabs, reducing deep traps, and identifying optimal spacers. The (111) series, which is defined as $A'_2A_{q-1}B_qX_{3q+3}$ $(q > 1)$, is obtained by sectioning along the body diagonal.[42] The activity in this orientation is limited by very high exciton binding energies, which hinder charge separation and subsequently reduce photovoltaic performance.

Compositionally, making specific compositional substitutions within the crystal sublattices, the electronic bandgap of halide perovskites can be tailored. For example, substituting the A-site ion with larger alkylammonium species influences the covalency of the B–X bond, allowing for the gap to be adjusted as needed.[43–45] Since the metal–halide interaction controls frontier orbital alignment, modifying the B-site cation also modifies the edge between the valence and conduction bands. A variety of complementary strategies, including altering bond angles through steric distortion, performing octahedral tilting, and intentionally inducing lattice strain, have been employed to create optical windows tailored for emerging electronic and photonic platforms. A further route is provided by adjusting the size of crystallites or creating controlled quantum confinement in films, as size effects can alter the gap and emergent excitonic activity.[46–48] A recent study that examined photocurrent hysteresis clarified ion transport dynamics in high-performance perovskites. The presence of a slight external bias was observed to reverse photovoltaic polarity, independent of device architecture, precursor chemistry, fabrication solvent, or contact materials, highlighting the crucial role of mobile ionic species. The rapid transport is a result of very low defect-formation energies and low migration barriers, making the mechanism exceptionally responsive to environmental factors such as moisture, thermal cycling, and the history of illumination that occurs during device aging.[49–51] In matrices with fewer constraints, organic A-site cations tend to orient themselves. This collaborative movement, along with its naturally elevated ionic conductivity, broadens migration pathways, influences current–voltage hysteresis, and directly connects molecular orientation to ionic dynamics within the semiconductor framework.[52–54] Single-crystal halide perovskites produced through slow cooling or inverse temperature crystallization exhibit reduced point defect densities and lack grain boundaries.[33,55,56] As a result, the energy needed for ion migration in dark conditions exceeds that of polycrystalline materials. Improved lattice integrity extends carrier lifetimes, reduces trap-mediated recombination, and enhances the stability of emissive quantum yield.[54,57,58] Moreover, higher obstacles impede drift currents even with prolonged bias application, maintaining electric fields.[59] While it is impossible to eliminate ion migration, enhancing crystallinity significantly reduces the number of mobile ions, indicating a hopeful path toward ensuring long-term device reliability while maintaining tunability.[60–62]

Also, the one-step deposition highlights the importance of controlled crystallization as a critical element in achieving perfect halide perovskite coatings, typically accomplished through spin coating or subsequent annealing.[55,63,64] At times, the loss of solvent, coupled with early crystal nucleation, leads to film contraction and disrupts the uniform development of layers. Through controlled solvent–antisolvent modulation, a homogeneous precursor matrix, produced by purposefully slowing nucleation, eventually converts. In contrast, accelerated crystallization utilizes brief anneal intervals instead of the prolonged growth duration dictated by the deferred route.[55,65,66]

Specifically, the volumetric expansion resulting from MAI diffusion into the PbI_2 lattice has become a crucial factor in process engineering.[67,68] Effective single-source vapor delivery of perovskite constituents relies on timely thermal input. As the increased current pushes the metal boat, its temperature rises sharply, causing the mixture to be removed in a rapid plume that later condenses on the cooler surface. The inorganic component requires intense heating to achieve rapid volatilization, while the associated organic component must concurrently remain below the thermal degradation threshold, a crucial measure. This ensures consistent phase purity and uniform coverage throughout extensive wafers.

3. Fundamental concepts and mechanisms of resistive switching in memory devices

The phenomena of resistive switching are typically attributed to two main mechanisms: electrochemical metallization (ECM) and the valence-change mechanism (VCM).[69,70]

In 2D halide perovskites, the ECM is characterized by the presence of active top electrodes, a sharp switching event at low bias that shows a significant dependence on compliance current(CC), narrow filament conductance, and a reset process achieved through dissolution when a reverse bias is applied. VCM is characterized by inert contacts, a gradual evolution of conductivity influenced by halide-vacancy drift and modulation of the interfacial barrier, symmetric or weakly asymmetric windows, and a more pronounced temperature/area scaling of high-resistance currents. Layered architectures influence mechanism selection by introducing anisotropic ion migration and spacer-dependent barrier heights. Vertical grain alignment stabilizes ECM filaments in the out-of-plane direction, while vacancy-ordered or single-crystal lattices increase migration barriers and encourage VCM-like, interface-limited responses. The density of defects and the order of the crystal structure

Open Access Article. Published on 03 octobre 2025. Downloaded on 2026-02-04 10:39:24.
This article is licensed under a Creative Commons Attribution 3.0 Unported Licence.

establish the nucleation landscape and the geometry of conductive paths in 2D lattices. Clusters of vacancies at grain boundaries or gaps induced by spacers initiate the formation of branched filaments, while vertically aligned, highly crystalline grains restrict growth to narrow channels that extend out of the plane, resulting in decreased variability. In ECM operation with Ag/Cu electrodes, the dissolving of cations within soft halide cages and the high mobility of cations along vertically oriented slabs contribute to reduced forming fields and a pronounced compliance-current dependence. Meanwhile, the dissolution process is influenced by local redox overpotential and heat dissipation at the counter electrode, resulting in a rapid and polarity-selective RESET. In VCM-dominated stacks, the generation and drift rates of vacancies are influenced by vacancy-formation energies, migration barriers, and interfacial band bending. Vacancy-ordered or single-crystal with low trap densities increases activation energies, reduces stochastic percolation, and promotes gradual, interface-limited switching, resulting in enhanced endurance.

In ECM configurations, the application of an electric field leads to the oxidation of the active electrode, resulting in the release of metal cations into the surrounding dielectric matrix for subsequent migration.[71] Upon emission, these cations navigate through the insulating layer and experience reduction at the inert counter-electrode, leading to the formation of conductive filaments that link the electrodes and lower resistance.[72–74] In the VCM action, anion vacancies, including oxygen or halide defects, act as the primary mobile entities.[75] Their movement through the dielectric changes the oxidation states of adjacent cations in the lattice, influencing conductivity *via* redox-driven valence modifications during real-time operation. ECM generally leads to sudden filament formation, while VCM can produce filamentary or interface-dominated responses that develop more gradually.[75–78] ECM mechanisms primarily control the switching behavior of cells with electrochemically active top electrodes.[79] The SET action is developing with a slight positive preference, as indicated by a sudden current increase that marks the beginning of filament growth.

On the other hand, RESET, under negative bias, breaks down the filament structure and quickly restores the material to its original HRS.[75,80] This phenomenon of sudden switching dominated by metallization is illustrated by designs utilizing silver (Ag) electrode layers. In contrast, gold (Au) electrode devices exhibit unique behavior, following a different mechanism that is solely regulated by interface processes. The generation of vacancies at the dielectric–electrode junction during forward bias leads to a reduction in depletion width, improves carrier transport, and results in an LRS for operation.

In the brain network, neurons function as the primary information-processing units, while minuscule connections, known as synapses, interconnect individual cells, creating extensive, coordinated circuits.[81,82] Upon detecting an electrical impulse, a presynaptic neuron undergoes membrane depolarization, generating a transient, all-or-nothing voltage pulse known as an action potential, which travels along the axon to the synaptic terminal.[83–85] Upon arrival, the spike activates calcium channels, facilitates vesicle fusion, and releases neurotransmitters that diffuse across the nanometer-wide cleft, prompting an electrical response in the postsynaptic membrane and ensuring precise point-to-point transmission.[84,86,87] This physiology motivates neuromorphic hardware. A synthetic synapse is typically constructed as a metal–insulator–metal configuration, where the top electrode represents the presynaptic side, the bottom electrode denotes the postsynaptic cell, and the intervening functional layer mimics the biological synaptic gap.[88,89] The conductance of this stack functions as synaptic weight, reflecting the coupling strength between adjacent elements; thus, the device resistance must encompass a range of intermediate values that allow precise weight modifications. Resistance tuning must be analog rather than binary, conductance states should be resilient yet responsive to submicrosecond inputs, and the platform should replicate both fundamental and composite plasticity rules with little energy expenditure.[88,90,91] Potentiation and depression require approximately symmetric and linear conductance modulation to enable consistent learning and mitigate random variation. Materials such as halide perovskites, phase change chalcogenides, and filamentary oxides achieve these objectives by regulating ion migration, facilitating reversible phase transitions, and manipulating nanoscale redox reaction.[92–95] Conventional central-processing designs segregate memory and logic, resulting in inefficiency in fulfilling these needs, but neuromorphic crossbars amalgamate memory with computation and function in parallel. Plasticity refers to alterations in transmission efficacy that are contingent upon neuronal activity. Potentiation enhances weight and conductivity, whereas depression diminishes them.[96,97] Temporal behavior occurs at several scales. Short-term potentiation (STP) and short-term depression (STD) refer to temporary alterations induced by individual spikes that dissipate as residual ions or trapped charges are eliminated.[98–100] Extended sequences of fast stimulation induce long-term potentiation (LTP) and long-term depression (LTD), resulting in modifications that persist from minutes to several hours and establish the foundation for enduring memory.[101,102]

Practically, memristive data storage utilizes two-terminal switching devices arranged in tightly packed crossbar matrices.[103] Each matrix comprises four elements: a driven word line, a grounded bit line, a nonlinear selector that reduces sneak-path leakage, and the memristive switch itself.[104,105] At every word-bit intersection, the selector (S), in conjunction with the resistive switching element (R), creates a 1S1R cell.[106,107] When the applied bias is beyond the selector threshold, current flows through the memristor, modifying its conductance. In the sensing phase, the device's resistance is compared with an external reference, and the resulting voltage division signifies the stored logic value. However, in physical networks, the simplicity of word- and bit-line addressing is undermined by channels that redirect current from the designated junction.[108–110] The lateral sharing of metallic rails results in several unexpected pathways traveling through unselected elements that share those rails. Memristive elements store data in a conductance level that changes according to the accumulated charge or flux encountered

© 2026 The Author(s). Published by the Royal Society of Chemistry

Open Access Article. Published on 03 octobre 2025. Downloaded on 2026-02-04 10:39:24. This article is licensed under a Creative Commons Attribution 3.0 Unported Licence.

by the device. The speed and energy advantages render memristors appealing for embedded computing designs. Diverse technologies achieve various resistance states *via* unique microscopic mechanisms. A prevalent technique alters the width, length, or composition of nanoscale conductive filaments. Another modifies the distance of an insulating tunneling gap, resulting in analog switching while incurring significant nonlinear *I–V* characteristics due to the exponential dependence of tunneling current on gap distance.[111–114] Among the existing approaches, compositional reconfiguration within the conductive pathway is considered a dependable method for achieving stable analog states. Continuous conductance tuning enables multiply-and-accumulate operations, allowing for concurrent vector–matrix multiplication within the array. In large-area fabrication, the 1 Transistor–1 Resistor (1T–1R) architecture, which pairs each memristor with a MOSFET, is the most viable manufacturing approach.[115–118] The access transistor reduces leakage in non-addressed cells, ensuring predictable write and read operations.

Nonetheless, the silicon space allocated to the transistor and its inactive power consumption generate interest in passive crossbars, where per-cell selectors are excluded to optimize areal density. Such passive layouts, however, encounter half-select disruptions and widespread sneak-path leaks that decrease inference accuracy and online learning. Engineers customize the memristor's *I–V* characteristics, incorporating significant nonlinearity or intrinsic rectification to ensure that OFF-state currents remain minimal without the need for supplementary devices.[119–121] A very adaptable solution incorporates a tiny selector in series with each junction, allowing ohmic behavior within the operating range while enforcing sharp rectification beyond that range.[122,123] The crossbar design automatically connects all rows and columns, and this parallel wiring promotes inadvertent conduction through neighboring sites that share a conductor with the selected location. Thus, the specified junction is biased in parallel with an undefined resistance formed by adjacent quiescent cells. The current crossing the unwanted branch disrupts the voltage divider and generates sneak leakage, which ultimately compromises the dependable operation of passive crossbars that lack specialized isolation.[124–127]

Interconnected chemo-ionic processes influence the stability of environmental and operational factors in 2D halide-perovskite memristors. These include moisture-assisted hydrolysis of organic spacers, halide loss due to bias or illumination, corrosion of electrodes, and diffusion of metals, as well as field-accelerated aggregation of vacancies that leads to phase segregation and shifts in interfacial band structure. The arrangement of crystalline structures and the orientation of vertical textures effectively reduce the channels for percolative ingress and restrict the lateral movement of ions. Additionally, the process of defect passivation at surfaces and grain boundaries prevents trap-assisted redox reactions, which would otherwise expand switching distributions and compromise retention. The approach involves utilizing hydrophobic or fluorinated spacer chemistry, implementing diffusion-barriered and chemically robust contacts, incorporating ionic-blocking or dipole-tuned interlayers, and applying conformal encapsulants that prevent water and oxygen ingress while stabilizing volatile halides during extended bias and thermal cycling.

4. Quasi-2D halide perovskite-based memory devices

Recently, 2D layered perovskites have been utilized in perovskite-based memory devices due to their enhanced thermal stability in comparison to 3D perovskites. The observed outcome can be attributed to the hydrophobic organic spacers that protect the perovskite layers from moisture and oxygen exposure.

Quasi-2D refers to Ruddlesden–Popper or Dion–Jacobson perovskites characterized by inorganic slabs of $n \geq 2$ that are separated by bulky organic spacers, resulting in electronically coupled layers with out-of-plane ionic confinement. In addition to PEA-based RP phases, notable examples include fluorinated spacers, branched or cyclic ammoniums, and DJ phases created by short diammonium linkers, all of which enhance vertical grain alignment and moisture tolerance, beneficial for achieving low-variability switching. Additional variants, mixed-halide I/Br lattices for filament tuning, Cu-based A_2BX_4 layers for lead-lean compositions, and 2D/3D stacked heterostructures expand the strategy space toward lower forming voltages, selector-free rectification, and multilevel conductance. In addition to their stability, various groups have proposed that 2D layered perovskites serve as promising candidates for memory devices due to their superior ON/OFF ratio, enhanced reliability, and reduced operating voltage.

Kim *et al.* evaluated the differences in switching behaviors constructed on $PEA_2MA_4Pb_5I_{16}$ layers with arbitrary orientation and those featuring well-aligned vertical grains.[128] Vertically oriented $PEA_2MA_4Pb_5I_{16}$ films were synthesized by including MACl as a directing additive during the deposition process. 8×8 crossbar arrays (Au/$PEA_2MA_4Pb_5I_{16}$/ITO) for systematic testing using a combination of traditional photolithography and electron-beam patterning. The top electrode, approximately five μm in width, was drawn up using conventional lift-off photolithography, the perovskite region (~600 μm) was defined using top-down exposure, and the top electrode, similarly 5 μm wide, was created *via* e-beam lithography. We subsequently analyzed the resistive switching behavior in arrays constructed from randomly oriented and vertically oriented films. The vertically aligned devices required a substantially lower electric field for electroforming (393 kV cm^{-1}) than their randomly oriented device (501 kV cm^{-1}). Moreover, the distributions of SET and RESET fields, together with LRS and HRS, were narrowed for vertically oriented films. This enhancement is ascribed to less variation in energy barriers for iodide-vacancy migration along the linear, vertically oriented conduction channels.

Additionally, Kim *et al.* $(PEA)_2MA_3Pb_4I_{13}$ as the resistive-switching layer seen in Fig. 3(a).[72] The $(PEA)_2MA_3Pb_4I_{13}$ films were fabricated using spin-coating. Fig. 3(b) illustrates the *I–V*

Open Access Article. Published on 03 octobre 2025. Downloaded on 2026-02-04 10:39:24.
This article is licensed under a Creative Commons Attribution 3.0 Unported Licence.

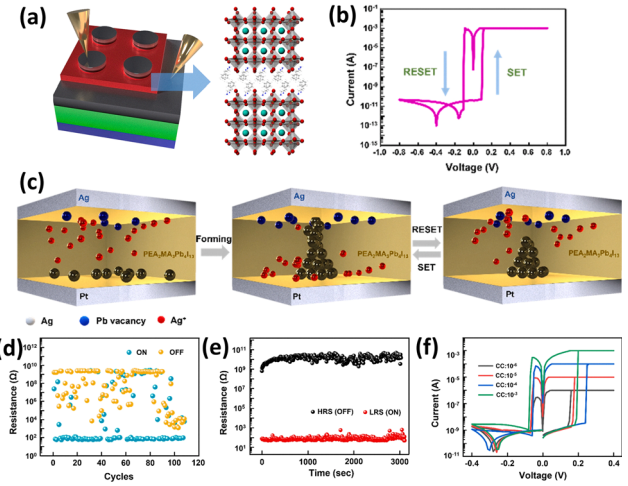

Fig. 3 (a) Schematic representation of the structure of the resistive switching memory device and the resistive switching materials $(PEA)_2MA_3Pb_4I_{13}$. (b) *I–V* characteristics of an Ag/$((PEA)_2MA_3Pb_4I_{13}$/Pt) device derived from five sequential voltage sweeps. (c) Schematic representation of the ECM mechanism. (d) Endurance characteristics for the $(PEA)_2MA_3Pb_4I_{13}$ memory device. (e) Retention duration of the ON and OFF states. (f) *I–V* characteristics of an Ag$(PEA)_2MA_3Pb_4I_{13}$/Pt device under four distinct CC. Reproduced with permission.[72] Copyright 2024, Elsevier.

characteristics, exhibiting bipolar switching with ON and OFF transitions occurring under opposing bias. The initial current spike followed by a stable LRS indicates filament production when the CC is restricted to 10^{-3} A. Imposing a negative bias fractures these filaments, restoring the device to an HRS with a current capacity of 10^{-2} A. The SET and RESET thresholds were +0.09 V and −0.10 V, respectively. The immaculate device initially conducted 10^{-11} A, but its current surged to 10^{-3} A when the bias over the SET threshold, resulting in an ON/OFF ratio of 10^8. Fig. 3(c) illustrates a filamentary ECM configuration for the $(PEA)_2MA_3Pb_4I_{13}$-based device. In a positive bias, Ag dissolves; its cations migrate toward the inert bottom electrode and are ultimately reduced, crystallizing at the interface. Fig. 3(d) illustrates endurance, indicating that 640 μs write/erase pulses of +0.8 V and −0.8 V, accompanied by a 0.05 V readout, maintained functionality for 100 cycles. Fig. 3(e) evaluates retention. Both states remained distinct for over 3000 s when read at 0.02 V, exhibiting only little HRS drift and negligible LRS degradation. Multilevel switching, examined for data density, is illustrated in Fig. 3(f). Modifying the CC from 10^{-3} A to 10^{-6} A resulted in four consistent LRS, while the HRS remained relatively unchanged. A single $(PEA)_2MA_3Pb_4I_{13}$ element can accommodate multiple resistance levels within a single junction, thereby enhancing storage capacity.

Also, Kim *et al.* achieved vertically aligned perovskite films within a 7 × 7 flexible crossbar array.[129] Vertically oriented $BA_2MA_5Pb_6I_{19}$ layers were synthesized by adjusting the precursor ratio (n = 6) in conjunction with SCN^- ion additions, resulting in humidity resistance over an entire calendar year in ambient conditions. The device exhibited a remarkable ON/OFF ratio of 10^7, exceptionally low SET and RESET voltages ($|V| < 0.15$), consistent device-to-device performance, outstanding durability of 5×10^6 cycles, and retention lasting 2×10^5 s. This performance results from pre-organized vertical 2D perovskite conduits, devoid of grain boundaries between the top and bottom electrodes, which stabilize conducting filaments within the ultrathin film and enable disturbance-free operation, thus enhancing dependability. Additionally, large hydrophobic organic cations impede water penetration into the inorganic framework, resulting in moisture stability lasting over 12 months. A 7 × 7 crossbar array demonstrating uniformity among elements was shown for nonvolatile data storage and on-demand reconfiguration. Pixel-scale images were input into the network and subsequently reconfigured to encode other visuals. Chen *et al.* reported an $(PEA)_2MAPb_2I_3Br_4$ based resistive switching memory,[130] fabricated entirely in air through a single-step spin-coating method, which is free of antisolvent steps and demonstrated excellent, repeatable bipolar switching. The quasi-2D perovskite layer facilitated SET operation at approximately 0.8 V, achieving an ON/OFF current window close to 10^4, all while maintaining over one thousand write–erase cycles without any signs of deterioration. Transport analysis revealed that space-charge-limited current is predominant in the high-resistance branch, while metallic-filamentary Ohmic flow takes over following the switching process. The PEA spacer provides hydrophobic protection, enabling stable resistive behavior at 40% relative humidity for over 90 days.

5. A_2BX_4 halide perovskite-based memory devices

Among various candidates, copper(II) can form a 2D layered perovskite similar to 2D lead halide perovskites. While Cu-based materials have been predominantly explored in the solar cell domain, there has been no effort directed toward their application in resistive switching memory. Given that Cu(II) possesses a 3d electronic configuration, the presence of octahedral Cu(II) in 2D layered perovskites could influence the switching mechanism as a result of alterations in the local geometry.

Kim *et al.* reported resistive switching in layered $(BzA)_2CuBr_4$ ($BzA = C_6H_5CH_2NH_3$), attaining significant memory devices.[131] The X-ray diffraction analysis of the spin-cast layer reveals pronounced (00*l*) reflections, indicating a specific orientation about the Pt bottom contact. A stack consisting of Ag/PMMA/$(BzA)_2CuBr_4$/Pt functions as a bipolar switching device. An initial electroforming event occurs around +0.5 V, followed by consistent SET and RESET operations at +0.2 V and −0.3 V. *I–V* sweeps demonstrate an ON/OFF ratio nearing 10^8, with cycling endurance surpassing 2000 repetitions and non-volatile retention extending beyond 1000 s. Multistate storage capability is confirmed when the CC is adjusted to provide intermediate conductance values. The analysis of conduction associates the LRS with ohmic filament channels, while the HRS is characterized by Schottky emission, aligning with an electrochemical metallization mechanism. Environmental stability

© 2026 The Author(s). Published by the Royal Society of Chemistry

Open Access Article. Published on 03 octobre 2025. Downloaded on 2026-02-04 10:39:24.
This article is licensed under a Creative Commons Attribution 3.0 Unported Licence.

tests conducted at 50% relative humidity over 14 days indicate minimal degradation, confirming that $(BzA)_2CuBr_4$ retains its structural and electronic integrity.

Kundar *et al.* investigated the use of bulky organic tetraethylammonium (TEA) ions to construct 2D $(TEA)_2PbBr_4$ and $(TEA)_2PbI_4$ layers for resistive switching memory devices.[132] The resultant 2D-structured devices exhibited bipolar resistive switching, with high ON/OFF ratios of 3×10^3 for $(TEA)_2PbBr_4$ and 8.83×10^3 for $(TEA)_2PbI_4$, while maintaining data retention exceeding 10^4 s and demonstrating substantial cycle durability. Furthermore, dependable switching continued at high temperatures nearing 400 K operation. Electrical transport studies indicated that Schottky emission predominated in the HRS, while Ohmic behavior was prevalent in the LRS domain of the devices. Notably, $(TEA)_2PbBr_4$-based memories required reduced SET voltages compared to their I counterparts, indicating their potential to substantially decrease total device power consumption during standard write–erase cycle operations. Moreover, the Br version exhibited consistent switching for 45 days, demonstrating its exceptional durability.

Integrating resistive-state modulation with intrinsic rectification in a single memory device can facilitate accurate write and read operations within a compact configuration. Nevertheless, achieving this dual capability at low bias remains challenging. Son *et al.* presented a self-rectifying memory that relies on a singular functional layer, which independently experiences lateral phase separation into ferroelectric poly(vinylidene fluoride-*co*-trifluoroethylene) (P(VDF-TrFE)) domains and BA_2PbI_4 in Fig. 4(a).[133] A consistent P(VDF-TrFE):BA_2PbI_4 composite layer was quickly deposited using straightforward spin casting. The P(VDF-TrFE):BA_2PbI_4 film comprises phase-separated BA_2PbI_4 within the P(VDF-TrFE) matrix, as illustrated in Fig. 4(b) and (c). The P(VDF-TrFE) polymer chains achieve self-alignment by strong intermolecular interactions with BA_2PbI_4 during phase separation in Fig. 4(d). The electrical analysis of Ag/P(VDF-TrFE):BA_2PbI_4/ITO device was conducted within a limited voltage range of ±0.4 V in Fig. 4(e). A transition to the LRS occurred at +0.32 V during the sweep from 0 to +0.4 V, accompanied by a current of approximately 10^{-5} A. Reversing the sweep from +0.4 V to −0.4 V RESET the device to the HRS, the OFF current remained below 10^{-11} A, resulting in an LRS/HRS ratio almost equal to 10^6. The *I*–*V* curve demonstrated asymmetry, achieving a rectification ratio of 10^6 at ±0.1 V, with current flowing solely under forward bias, while reverse-bias conduction was significantly reduced. The stable preservation of both states surpassed 10^4 s, and dependable switching continued for 200 consecutive cycles Fig. 4(f) and (g). The observed behavior is ascribed to the electrochemical doping of BA_2PbI_4 by migrating Ag^+ species, as schematically depicted in Fig. 4(h). No switching was observed when the active Ag electrode was replaced with an electrochemically inert metal, even under higher voltage conditions. The operating voltages conform to the tolerance limits of peripheral circuits, minimizing energy consumption and Joule heating.

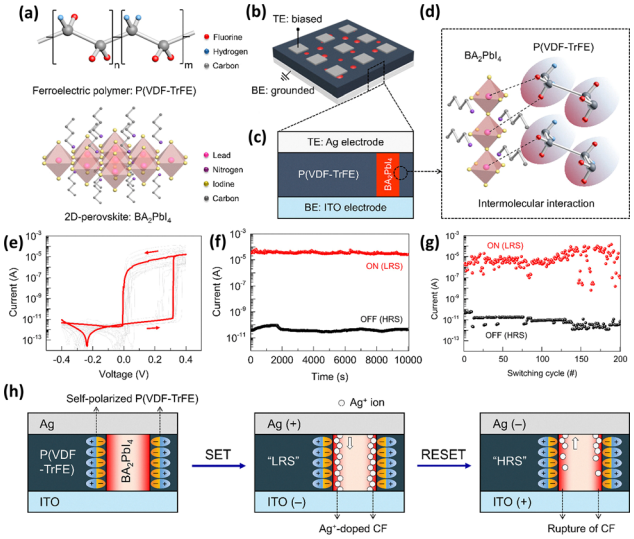

Fig. 4 (a) Diagrams showing the molecular configurations of the ferroelectric P(VDF-TrFE) polymer and BA_2PbI_4 2D perovskite. (b) Diagram of a resistive memory device architecture and (c) cross-sectional view of the device illustrating a phase-separated lateral heterostructure comprising the BA_2PbI_4 crystal embedded within a P(VDF-TrFE) matrix, positioned between upper Ag and lower ITO electrodes. (d) Diagram of the P(VDF-TrFE) and BA_2PbI_4 interface, illustrating the self-orientation of P(VDF-TrFE) chains due to intermolecular interactions with BA_2PbI_4, resulting in lateral ferroelectric polarization. (e) Resistive switching *I*–*V* characteristics of the Ag/P(VDF-TrFE):BA_2PbI_4/ITO device. The red arrows indicate the direction of the scan. The *I*–*V* curves from twenty devices are displayed beside the grayscale. (f) Retention time and (g) endurance cycle of LRS and HRS. (h) Schematic representation of the resistive switching mechanism. P(VDF-TrFE) is first self-polarized at the P(VDF-TrFE):BA_2PbI_4 contact. After setting, Ag^+ ions traverse the P(VDF-TrFE):BA_2PbI_4 interface and dope BA_2PbI_4, leading to the emergence of localized Ag^+-doped conductive filaments. Following the reset, the Ag^+-doped conducting filaments are broken. Reproduced with permission.[133] Copyright 2025, American Chemical Society.

6. ABX_4 halide perovskite-based memory devices

The significance of grain boundaries in resistive switching memory devices lies in their role during the switching operation, which is made easier by ion migration. These grain boundaries can serve as methods that enhance the migration process. Controlling the grain size has the potential to influence the memory characteristics of devices. To attain a high-performance memory device, it is essential to regulate the grain size within the film.

Park *et al.* employed 3-(aminomethyl)piperidinium (3AMP) as the organic spacer cation was synthesized for (3AMP)-PbI_4, as illustrated in Fig. 5(a).[134] The morphology of the grains was modified by varying the relative volumes of *N*,*N*-dimethylformamide (DMF), and dimethyl sulfoxide (DMSO) in the precursor mixture. Three representative solutions, DMF : DMSO = 1 : 0, 1 : 1, and 0 : 1, produced films illustrated in Fig. 5(b)–(d). The increase in DMF fraction led to a gradual decrease in crystalline domain size. The electrical traces presented in Fig. 5(e) indicate that processing with a DMF-rich environment leads to an increase

Open Access Article. Published on 03 octobre 2025. Downloaded on 2026-02-04 10:39:24.
This article is licensed under a Creative Commons Attribution 3.0 Unported Licence.

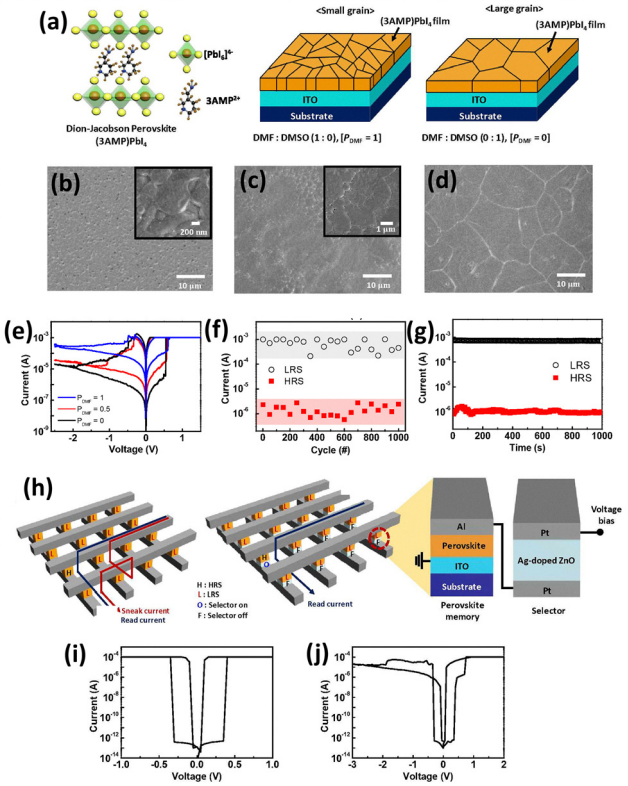

Fig. 5 (a) Schematic illustration of (3AMP)PbI_4 with atom colors indicated: Pb in red, I in yellow, C in black, N in blue, and H in orange. A schematic illustration of the grain size-controlled (3AMP)PbI_4 films is presented. SEM images of (3AMP)PbI_4 films deposited using solutions with (b) PDMF : DMSO = 1 : 0, (c) PDMF : DMSO = 1 : 1, and (d) PDMF : DMSO = 0 : 1 are presented. (e) *I–V* characteristics of the devices exhibiting varying grain sizes. (f) Evaluation of cycling endurance of the device subjected to repeated SET pulse applications (2 V, 10 ms) and RESET pulse applications (−3 V, 10 ms). (g) Data retention characteristics of the device. Measurements of all current levels at the HRS and LRS were conducted at a read voltage of 0.2 V. (h) Schematic illustration depicting the sneak-path current within a cross-point memory array. A schematic illustration of a device connected to an Ag-doped ZnO-based selector device featuring a 1S1R configuration. *I–V* characteristics of (i) the selector device and (j) the device linked to the selector device. Reproduced with permission.[134] Copyright 2022, American Chemical Society.

in the HRS current, resulting in a reduction of the ON/OFF window. The examination of reliability involved the use of repetitive pulse sequences. Positive pulses of +2 V for 10 ms successfully carried out the designated action, whereas negative pulses of −3 V for 10 ms accomplished the RESET. Fig. 5(f) illustrates sustained functionality over 1000 cycles without any observable decline, indicating that grain-size management allows reliable performance. The retention data in Fig. 5(g) demonstrate consistent HRS and LRS currents throughout 1000 s, thus affirming remarkable data stability. In crossbar array, stray currents in non-addressed cells interfere with precise reading from the intended junction, as shown in Fig. 5(h). A threshold selector element was integrated to restrict this conduction. The standalone selector demonstrated bidirectional threshold characteristics, featuring an off-state current close to 1×10^{-12} A and a selectivity of approximately 1×10^{8} in Fig. 5(i); upon the removal of bias, conductive filaments dissolved as Ag reverted to ionic form, resulting in a decrease in surface energy. A one-selector–one-resistor (1S1R) stack was illustrated by linking the Al contact of the memory cell to the Pt bottom electrode of the selector, followed by the application of voltage to the selector's Pt top electrode. In the course of a forward sweep in Fig. 5(j), the selector activated at 0.3 V, allowing for the subsequent setting action of the memory element at 0.8 V. During the reverse sweep, the selector activated at −0.3 V, subsequently leading to a gradual RESET.

Khemnani *et al.* reported that 3,4-ethylene dioxythiophene-polystyrene sulfonate (PEDOT:PSS) and poly(methyl methacrylate) (PMMA) were positioned at the ITO/(3AMP)–PbI_4/Ag interfaces, respectively.[135] Fig. 6(a) illustrates the *I–V* characteristics of the ITO/PEDOT:PSS/halide perovskite/PMMA/Ag device, demonstrating an ON/OFF ratio of around 10^3. The threshold necessary for SET operation decreases to 0.33 V, far lower than the 0.8 V recorded. The nonlinear, asymmetric *I–V* curve depicted in Fig. 6(b) reflects the characteristics of a self-rectifying memory element. Self-gating cells are candidates for compact, energy-efficient neuromorphic devices due to their intrinsic rectification, which reduces sneak-path leakage in cross-point lattices and reduces read errors. The incorporation of interlayers significantly enhances device durability, achieving 100 switching cycles and 6000 s of retention, as illustrated in Fig. 6(c). A series of presynaptic stimuli (1 V amplitude, 0.1 ms interspike interval, 100 ms pulse width, 0.2 V read) was administered to demonstrate gradual potentiation. The gradual increase in synaptic weight indicates learning ability, while the elimination of the initial gain typifies the erasure process depicted in Fig. 6(d). A second learning process is confirmed when the weight is raised to a higher plateau after reapplying the same training. The process of cycling between learning,

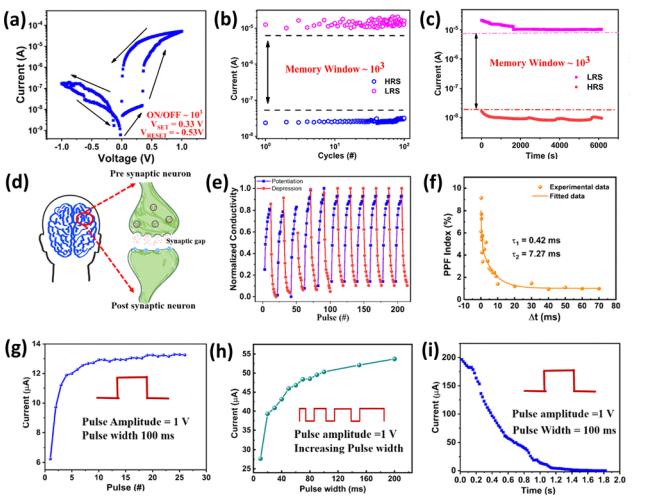

Fig. 6 (a) The *I–V* characteristics, (b) endurance, and (c) retention time of the fabricated ITO/PEDOT:PSS/active layer/PMMA/Ag device are presented, respectively. (d) Human brain featuring pre- and postsynaptic neurons, (e) characteristics of learning and forgetting mechanisms, (f) SNDP, (g) PPF index, (h) IPSC, and (i) EPSC. Reproduced with permission.[135] Copyright 2023, American Chemical Society.

© 2026 The Author(s). Published by the Royal Society of Chemistry

Open Access Article. Published on 03 octobre 2025. Downloaded on 2026-02-04 10:39:24. This article is licensed under a Creative Commons Attribution 3.0 Unported Licence.

forgetting, and relearning ultimately saturates the load. Interneuronal coupling can be adjusted by modifying the spike interval, pulse count, or width; the associated plasticity mechanisms include paired-pulse facilitation (PPF), spike-number-dependent plasticity (SNDP), and excitatory postsynaptic current (EPSC). In biological circuits, PPF promotes swift information processing and memory consolidation. Upon the arrival of an initial excitation at a presynaptic terminal, ionic influx occurs. Restoration to baseline requires a finite duration; a subsequent identical stimulation during this recovery produces a greater response, hence establishing paired-pulse facilitation (PPF). Fig. 6(e) illustrates that the PPF index reduces as the interspike delay (Δt) increases, exhibiting a rapid component of 0.42 ms (τ_1) and a gradual component of 7.27 ms (τ_2). Plasticity contingent upon spike quantity also arises: Fig. 6(f) demonstrates that increasing the number of presynaptic pulses from 1 to 25 consistently enhances device conductance. Width-dependent modulation was investigated by extending pulse durations from 10 ms to 200 ms, resulting in an increase in conductivity from 27 μA to 54 μA, as illustrated in Fig. 6(g). Inhibitory postsynaptic currents (IPSCs) in biological neurons occur when neurotransmitters released from presynaptic neurons bind to inhibitory receptors, resulting in a reduction in inward charge flow. A memristive analog exhibits a reduction in channel current with targeted stimulation (100 ms duration, 1 V amplitude) in Fig. 6(h), accurately replicating inhibitory neurotransmission. Fig. 6(i) documents an IPSC duration of 1 s for the ITO/PEDOT:PSS/(3AMP)–PbI_4/PMMA/Ag configuration.

7. $A_3B_2X_9$ halide perovskite-based memory devices

The perovskite-like compounds $A_3B_2X_9$ have predominantly captured attention thus far. This specific category of lead-free perovskites has a structure derived from ABX_3 *via* a combinatorial method and is recognized to exist in two distinct polymorphs: a 0D dimer phase and a 2D layered phase, with the dimer phase being thermodynamically favored. Nonetheless, the current initiatives involving these $A_3B_2X_9$ perovskites in memristor applications have predominantly concentrated on the dimer phase.

Paramanik *et al.* demonstrated the resistive switching properties of 2D layered $Cs_3Sb_2I_9$ perovskite thin films for application in memristive and neuromorphic devices.[136] The defect-ordered $Cs_3Sb_2I_9$ was synthesized using a vapor-assisted solution method, and a comprehensive structural investigation confirmed high phase purity in the deposited layers. Schottky designs exhibited consistent, non-volatile, bipolar switching at an exceptionally low voltage of 0.4 V, attaining an ON/ OFF ratio close to 10^4, data retention beyond 10^4 s, cycling endurance of 100 cycles, and remarkable sustainability. In contrast, sandwich devices provided a unique optical readout derived from the open-circuit voltage (V_{OC}) resulting from significant light-matter coupling within the perovskite framework. Furthermore, in spiking-rate-dependent plasticity trials, the devices exhibited short-term plasticity in conjunction with sustained long-term potentiation, thereby indicating viable learning processes.

Also, Yuan *et al.* explored the synthesis of lead-free, all-inorganic $Cs_3Sb_2I_9$ perovskite layers with high environmental durability using a hydrochloric-acid-assisted solution route at low temperatures.[138] The integration of Ag/PMMA/$Cs_3Sb_2I_9$/ITO stacks resulted in devices exhibiting consistent bipolar resistive switching. The optimized memories function at around −0.34 V for SET and +0.25 V for RESET, achieving an ON/OFF window near 66 and maintaining performance for a minimum of 120 switching cycles while keeping stored states for over 10^4 s. Flexibility examinations indicate minimal performance decline when substrates are subjected to various bending radii or cycled 1000 times, emphasizing their mechanical durability. Moreover, the resistive-switching characteristics demonstrate stability even after over 10 days of exposure to ambient air, confirming long-term chemical stability.

Ge *et al.* assess dense 0D $Cs_3Bi_2I_9$ and layered 2D $CsBi_3I_{10}$ films exhibiting homogeneous surface morphology.[137] Following the deposition on chemically cleaned FTO glass, high-purity Ag electrodes were thermally evaporated onto the $Cs_3Bi_2I_9$ and $CsBi_3I_{10}$ layers, resulting in the formation of sandwich-type devices depicted in Fig. 7(a). Cross-sectional SEM images seen in Fig. 7(b) and c confirm the layered structure, indicating film thicknesses of approximately 1.1 μm for $Cs_3Bi_2I_9$ and 0.6 μm for $CsBi_3I_{10}$. The evaporation of the electrode simultaneously produces a thin AgO_x interphase, an essential characteristic for resistive switching, which will be analyzed in the subsequent explanation of the mechanism. The resistive-switching behavior of $Cs_3Bi_2I_9$ and $CsBi_3I_{10}$ was examined by varying the top Ag electrode voltage from 0 to −2.0 V, returning to 0, increasing to 1.5 V, and ultimately returning to 0 V under ambient conditions. The typical *I–V* curves depicted in Fig. 7(d)–(g) for $Cs_3Bi_2I_9$- and $CsBi_3I_{10}$-based devices demonstrate clear, reproducible bipolar switching with minimal hysteresis drift. The SET operation, specifically the transition from HRS to LRS, is initiated during the negative bias phase without an external current limiter. A subsequent positive bias initiates the reset event, consistently restoring both $Cs_3Bi_2I_9$ and $CsBi_3I_{10}$ from LRS to HRS within a limited voltage range. The switching durability in Fig. 7(e)–(h) and retention behavior in Fig. 7(f)–(i) were meticulously assessed at a read voltage of −0.04 V for statistically independent devices. Both compositions maintained consistent HRS–LRS cycling for a minimum of 250 cycles, achieving a very high ON/OFF ratio close to 10^6 without encapsulation. This ratio significantly exceeds the previously recorded value for a $CsBi_3I_{10}$ device utilizing an Al electrode, demonstrating the critical impact of architecture on performance enhancement. A significant interface barrier resulting from the work-function disparity between perovskite and metallic contacts is advantageous for optimizing the ON/OFF ratio by stabilizing the off state. Moreover, the intrinsically elevated resistivity of these low-dimensional lattices, due to isolated octahedral complexes, effectively decreases OFF current and, therefore, enhances the ON/OFF ratio. The $Cs_3Bi_2I_9$ device sustains its on-state for over 10^3 s under continuous read

Open Access Article. Published on 03 octobre 2025. Downloaded on 2026-02-04 10:39:24.
This article is licensed under a Creative Commons Attribution 3.0 Unported Licence.

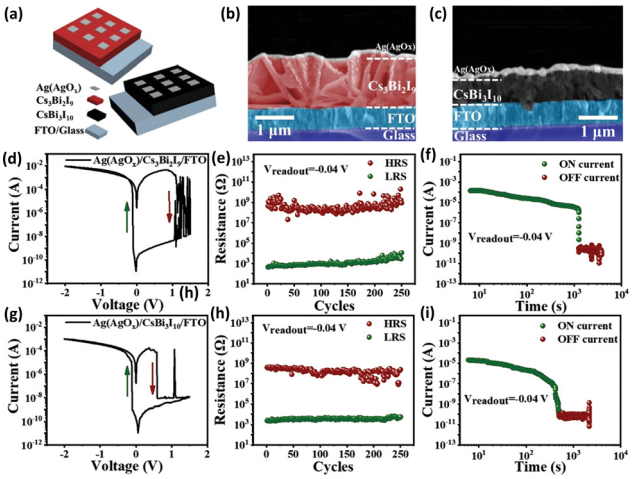

Fig. 7 (a) Schematic representation of devices based on $Cs_3Bi_2I_9$ and $CsBi_3I_{10}$. Cross-sectional SEM pictures of (b) $Cs_3Bi_2I_9$ and (c) $CsBi_3I_{10}$ device architectures, presented in false color, respectively. (d) Characteristic *I*–*V* curve of the $Cs_3Bi_2I_9$-based device presented in a semilogarithmic scale, accompanied by (e) switching endurance and (f) retention test results. Characteristic (g) *I*–*V* curve, (h) switching endurance, and (i) retention data of the $CsBi_3I_{10}$-based device, respectively. Reproduced with permission.[137] Copyright 2020, Wiley.

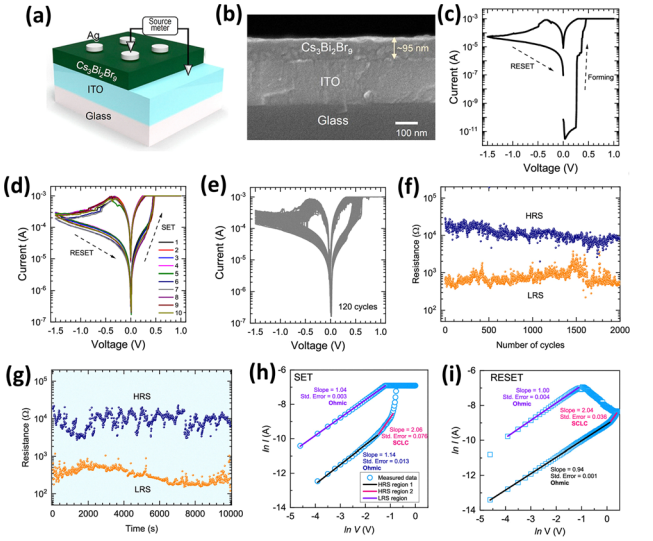

Fig. 8 (a) Schematic representation of a resistive switching device including an Ag/$Cs_3Bi_2Br_9$/ITO/glass configuration. (b) Cross-sectional scanning electron microscopy (SEM) image depicting the 95 nm thick $Cs_3Bi_2Br_9$ film. *I*–*V* characteristics for (c) the first switching phase, illustrating the forming step; (d) the subsequent 10 sweeps; and (e) the 120 cycles after the forming step. Bias voltages of +1.0 V were applied for the formation and SET processes, while −1.5 V was utilized for the RESET process in the Ag/$Cs_3Bi_2Br_9$/ITO devices. (f) Endurance and (g) retention duration of the Ag/$Cs_3Bi_2Br_9$/ITO device were assessed with a bias voltage of +1.0 V for the SET process and −1.5 V for the RESET operation, with a CC of 10^{-3} A. The voltage reading was +0.10 V, and the pulse duration was 100 μs. Natural logarithm of *I*–*V* data for (h) SET and (i) RESET procedures. Reproduced with permission.[139] Copyright 2022, American Chemical Society.

pulses, demonstrating enhanced retention compared to $CsBi_3I_{10}$. The extensive ON/OFF ratio allows multilevel switching, easily accomplished by adjusting CC during the SET process by simple compliance modulation.

Kim *et al.* all-inorganic $Cs_3Bi_2Br_9$ perovskite layers less than 100 nm in thickness were derived from pre-synthesized $Cs_3Bi_2Br_9$ powder, a technique that avoids the insufficient solubility that restricts the use of direct CsBr/$BiBr_3$ solutions.[139] The resistive switching was evaluated using the Ag/95 nm $Cs_3Bi_2Br_9$/ITO configuration, as depicted in Fig. 8(a) and (b). The dark current–voltage curve for the ultrathin film depicted in Fig. 8(c) demonstrates bipolar switching; the Ag/$Cs_3Bi_2Br_9$/ITO stack was subjected to a voltage sweep from 0 to +1.0 V for SET, followed by a sweep to −1.5 V for RESET, under a CC of 1 mA (10^{-3} A). After formation, 10 cycles adhered to the sequence of 0 V → +1.0 V → 0 V → −1.5 V → 0 V, as depicted in Fig. 8(d). A swift increase in compliance to approximately +0.45 V indicated filament formation and transition into the LRS, while the subsequent return sweep progressively restored the HRS. Fig. 8(e) verifies consistent switching over 120 cycles with an ON/OFF ratio of approximately 10^2. Fig. 8(f) illustrates that this ratio, which remains over 10, remains nearly constant during 1000 cycles and decreases only for an additional 1000 cycles, signifying endurance. The non-volatile operation is confirmed by the median resistance in both states remaining constant across a 10^4 s retention test. *I*–*V* graphs were analyzed to elucidate transport processes in Fig. 8(g). In the HRS low-field range of 0.02–0.22 V, a slope of 1.14 signifies Ohmic conduction by thermally activated electrons Fig. 8(h). Upon reaching the compliance limit, the log curve maintains a slope of 1.04, indicating that Ohmic behavior persists in the LRS. In the negative bias (RESET, Fig. 8(i)), the LRS exhibits Ohmic conduction with a slope of 1.00. Upon the device's reversion to HRS, a pronounced slope of 2.04 indicates a trap-controlled space-charge-limited current. A subsequent slope of 0.94 characterizes the recovered HRS, signifying a return to Ohmic transport following filament rupture.

The analysis of A_2BX_4, ABX_4, and $A_3B_2X_9$ devices reveals that the reactivity of the electrodes and the identity of the halides primarily determine the mechanism: active Ag/Cu contacts featuring iodide-rich lattices promote ECM with sharp, sub-volt set points and easily adjustable multilevel states. In contrast, inert electrodes and hosts with higher defect formation energies lead to responses that trend towards voltage-controlled mechanisms or interface-limited transport, characterized by wider switching windows and more pronounced temperature and area scaling. Dimensionality and morphology play crucial roles in determining OFF-state leakage and rectification. The presence of 0D dimer phases, such as $Cs_3Bi_2I_9$, effectively suppresses leakage and enhances retention stability. In contrast, polymer–perovskite phase-separation architectures, offer strong intrinsic rectification that is ideal for selector-free operation. Additionally, controlling grain size and using external threshold selectors continue to be effective strategies for ABX_4 films in crosspoint arrays, particularly in scenarios where sneak paths are prevalent. Bromide compositions typically reduce SET thresholds and enhance thermal and ambient robustness compared to iodides, while iodides tend to provide larger ON/OFF windows and allow for easier multilevel tuning.

© 2026 The Author(s). Published by the Royal Society of Chemistry

Open Access Article. Published on 03 octobre 2025. Downloaded on 2026-02-04 10:39:24.
This article is licensed under a Creative Commons Attribution 3.0 Unported Licence.

8. Single crystal and double halide perovskite-based memory devices

Kim *et al.* investigated that butylammonium (BA) spacer cations into the $Cs_2AgBiBr_6$ lattice results in the formation of a 2D $BA_2CsAgBiBr_7$, as confirmed by distinct (00*l*) reflections observed in powder X-ray diffraction patterns.[127] A 230-nm-thick $BA_2CsAgBiBr_7$ layer deposited on Pt and completed with Ag forms a vertical $Ag/BA_2CsAgBiBr_7/Pt$ stack that demonstrates distinct bipolar resistive switching. The device demonstrates an ON/OFF ratio nearing 10^7, with consistent SET and RESET at +0.13 V and −0.20 V, respectively. The endurance of the pulse exceeds 1000 cycles, and the non-volatile retention remains stable for a minimum of 2×10^4 s. Adjustable CC promotes distinct multilevel conductance states, indicating potential applications in analog memory and neuromorphic hardware. Transport analysis attributes high-resistance behavior to temperature-assisted Schottky emission and low-resistance behavior to ohmic conduction. Thermal stress at 85 °C and continuous exposure to ambient air for 22 days induce minimal degradation, confirming the strong operational durability of the $BA_2CsAgBiBr_7$ memory device.

Also, Jung *et al.* developed a single-crystal $CsPb_2Br_5$ resistive-switching memory device without grain-boundary interference, resulting in vertical devices that provide an ON/OFF ratio of approximately 1×10^8 while functioning below 0.32 V.[140] Furthermore, the device exhibited voltage-controlled multilayer functionality, preserving a significant resistance gap of roughly 1×10^2 between consecutive states. To clarify the switching mechanism, the research comprehensively compared resistive-switching responses across several geometries (vertical *versus* planar) and electrode chemistries (inert *versus* active). The results revealed that the drift of active-metal ions predominates the switching event, suggesting that the controlling mechanism can vary significantly with the crystallographic framework. Furthermore, the 2D structure, consisting of alternating Cs sheets and Pb_2Br_5 slabs, predominantly facilitates low-voltage multistate functionality in the single-crystal $CsPb_2Br_5$ vertical resistive-switching devices.

9. Conclusion

In conclusion, 2D halide perovskites have developed into attractive materials for sophisticated resistive memory. Layered Ruddlesden–Popper, Dion–Jacobson, vacancy-ordered, and single-crystal lattices provide dependable bipolar switching, exceptionally low SET voltages, and extensive ON/OFF ratios while maintaining mechanical flexibility and robust resistance to environmental deterioration. Comparative studies of solution-processed and vapor-grown films demonstrate that vertical crystal alignment, interface design, and suitable electrode selection reduce grain-boundary scattering, stabilize conductive filaments, and minimize sneak-path leakage.

The varied structural patterns examined here allow a wide array of device behaviors. Multilevel conductance states arise from regulated ion migration, allowing individual junctions to exhibit multiple resistance levels. Intrinsic rectification reduces leakage currents, enabling densely arranged passive crossbar arrays to function with remarkably low energy consumption. When subjected to inspired pulse sequences, these perovskite elements exhibit essential synaptic characteristics, including paired-pulse facilitation, short-term and long-term plasticity, and rate-dependent learning, thereby emphasizing their potential as artificial synapses in neuromorphic architectures.

Lead-free alternatives utilizing bismuth and antimony structures enhance durability and environmental suitability, whereas vacancy-ordered and single-crystal configurations reduce defect-mediated recombination and provide exceptional stability in retention. Spin-coated layers utilize solvent-controlled crystallization for consistent coverage, while vapor-deposited films offer wafer-scale uniformity and compositional regulation. Through these production methods, thin perovskite films exhibit remarkable endurance cycles and retain non-volatile states over extended durations.

The results obtained in this study demonstrate the ability of halide perovskites to incorporate memory storage, signal modulation, and synapse simulation in small devices. The ongoing improvement of composition, morphology, and device architecture is anticipated to improve performance metrics and broaden application prospects, establishing halide-perovskite memristors as fundamental elements in next-generation information-processing hardware.

Author contributions

Hyojung Kim: writing – original draft, funding acquisition.

Conflicts of interest

There are no conflicts to declare.

Data availability

No primary research results, software or code have been included and no new data were generated or analysed as part of this review.

Acknowledgements

This work was supported by the National Research Foundation of Korea (NRF) grant funded by the Korean government (MSIT) (RS-2025-00554803).

Notes and references

1 G. Li, M. Hilal, H. Kim, J. Lee, Z. Chen, B. Li, Y. Cui, J. Hou and Z. Cai, Selective CO_2 Detection at Room Temperature with Polyaniline/SnO_2 Nanowire Composites, *Coatings*, 2024, **14**, 1590, DOI: 10.3390/coatings14121590.
2 H. Kim, B. Kang and C. Moon, Refractive Index Modulation for Metal Electrodeposition-Based Active Smart Window

Open Access Article. Published on 03 octobre 2025. Downloaded on 2026-02-04 10:39:24. This article is licensed under a Creative Commons Attribution 3.0 Unported Licence.

Applications, *Micromachines*, 2024, **15**, 334, DOI: 10.3390/mi15030334.

3 J. Lee, H. Kim, M. Hilal and Z. Cai, Core–shell SnO_2/NiO p–n heterojunction composite for enhanced triethylamine gas sensitivity and selectivity, *J. Mater. Sci.: Mater. Electron.*, 2024, **35**, 1421, DOI: 10.1007/s10854-024-13196-x.

4 H. Kim, G. Veerappan and J. H. Park, Conducting Polymer Coated Non-woven Graphite Fiber Film for Dye-Sensitized Solar Cells: Superior Pt- and FTO-Free Counter Electrodes, *Electrochim. Acta*, 2014, **137**, 164–168, DOI: 10.1016/j.electacta.2014.06.012.

5 D. Shin, J. Lee, H. Pyo, S. Lee, H. Kang, H. Kim and C. W. Moon, Design strategies for electrochromic displays, *J. Korean Ceram. Soc.*, 2025, **62**, 575–610, DOI: 10.1007/s43207-025-00509-x.

6 J. Lee, H. Kim, M. Hilal and Z. Cai, Enhanced acetone gas sensor *via* TiO_2 nanofiber-NiO nanoparticle heterojunction, *Solid State Sci.*, 2024, **156**, 107683, DOI: 10.1016/j.solidstatesciences.2024.107683.

7 H. Kim, G. Veerappan, D. H. Wang and J. H. Park, Large Area Platinum and Fluorine-doped Tin Oxide-free Dye sensitized Solar Cells with Silver-Nanoplate Embedded Poly(3,4-Ethylenedioxythiophene) Counter Electrode, *Electrochim. Acta*, 2016, **187**, 218–223, DOI: 10.1016/j.electacta.2015.11.051.

8 G. Li, J. Hou, M. Hilal, H. Kim, Z. Chen, Y. Cui, J.-H. Kim and Z. Cai, Development of High-Performance Ethanol Gas Sensors Based on La2O3 Nanoparticles-Embedded Porous SnO_2 Nanofibers, *Sensors*, 2024, **24**, 6839, DOI: 10.3390/s24216839.

9 J. Lee, H. Kim, M. Hilal and Z. Cai, Efficient acetone sensing utilizing Co_3O_4-Embedded porous ZnO nanofibers, *J. Electroceram.*, 2024, **52**, 283–296, DOI: 10.1007/s10832-024-00367-9.

10 Z. Song, M. Hilal, H. S. Abdo, Z. Cai, H. Kim and J. I. Han, Synergistic ZnO–NiO composites for superior Fiber-Shaped Non-Enzymatic glucose sensing, *J. Ind. Eng. Chem.*, 2025, **144**, 691–699, DOI: 10.1016/j.jiec.2024.10.016.

11 M. Hilal, Y. Ali, H. Fayaz, Z. Cai, H. Kim, H. S. Abdo and I. A. Alnaser, Hierarchical Co_3O_4@ZnO binary oxide microstructures for high-performance photoelectrochemical glucose sensing, *Ceram. Int.*, 2025, **51**, 31545–31555, DOI: 10.1016/j.ceramint.2025.04.343.

12 J. Hwang, J. H. Chung, H. J. Kim, S.-H. Park, Y.-H. Cho, S. Sohn, S.-J. Ro, H. Kim, K. Lee, D. Cho, J. H. Seo, Y.-S. Shim, J. Lee and W. Lee, CeO_2/NiO heterostructures for extremly-selective acetone detection: The critical role of the Ce^{3+}/Ce4+ ratio in NiO nanodomes, *Sens. Actuators, B*, 2025, **442**, 138070, DOI: 10.1016/j.snb.2025.138070.

13 Y. Cho, D. Kim, J. H. Seo, J. H. Chung, Z. Park, K. C. Kwon, J. Ko, T. W. Ha, J. Lee, G. Kim, S. Ro, H. Kim, C. Lee, K. Lee, Y. Shim and D. Cho, Artificial Olfactory System Enabled by Ultralow Chemical Sensing Variations of 1D SnO_2 Nanoarchitectures, *Adv. Sci.*, 2025, **12**, 2501293, DOI: 10.1002/advs.202501293.

14 M. Hilal, Y. Ali, Z. Cai, H. Kim, H. S. Abdo, I. A. Alnaser and Y. Hwang, 3D flower-like Co_3O_4@ZnO nanostructures for trace-level acetone detection at low operating temperatures, *Sens. Actuators, A*, 2025, **388**, 116479, DOI: 10.1016/j.sna.2025.116479.

15 H. Yuan, M. Hilal, Y. Ali, H. M. U. Ayub, Z. Cai, H. Kim, W. Zhang, A. A. Khan, H. S. Abdo, I. A. Alnaser, Y. Hwang and J. I. Han, Synergistic charge transfer in 3D-V_2O_5/1D-Co_3O_4 composite for ultra-sensitive NO_2 gas detection, *Surf. Interfaces*, 2025, **58**, 105888, DOI: 10.1016/j.surfin.2025.105888.

16 H. Yuan, M. Hilal, Y. Ali, H. S. Abdo, Z. Cai, H. Kim, U. Ullah, H. Fayaz, W. Xie and J. I. Han, High-performance ZnO:CuO composite-based fiber-shaped electrode for non-enzymatic glucose sensing in biological fluids, *Surf. Interfaces*, 2024, **54**, 105266, DOI: 10.1016/j.surfin.2024.105266.

17 M. Hilal, Y. Ali, Z. Cai, H. Kim, H. S. Abdo, I. A. Alnaser and Y. Hwang, Synergistic MXene@NiO–ZnO heterostructures *via* dual-pressure hydrothermal synthesis for high-performance photoelectrochemical glucose sensing, *Ceram. Int.*, 2025, **51**, 16246–16256, DOI: 10.1016/j.ceramint.2025.01.465.

18 M. Hilal, Y. Ali, Z. Cai, H. Kim, H. S. Abdo, I. A. Alnaser, Y. Hwang and J. I. Han, Fabrication of electrochemically stable 3D V_2O_5/Nickel foam electrode with enhanced photoelectrochemical activity for high-performance glucose sensing, *Surf. Interfaces*, 2025, **60**, 106097, DOI: 10.1016/j.surfin.2025.106097.

19 Y.-J. Son, S.-W. Kim, H.-M. Kim, H. Kim, B. Chu and D.-Y. Jeong, Dielectric Properties of Composite PZT Films with Distinct Phase-Transition Temperatures *via* Aerosol Deposition, *Materials*, 2025, **18**, 1427, DOI: 10.3390/ma18071427.

20 C. Katan, N. Mercier and J. Even, Quantum and Dielectric Confinement Effects in Lower-Dimensional Hybrid Perovskite Semiconductors, *Chem. Rev.*, 2019, **119**, 3140–3192, DOI: 10.1021/acs.chemrev.8b00417.

21 A. Velasquez and S. K. Jha, in 2014 9th International Design and Test Symposium (IDT), IEEE, 2014, pp. 147–152.

22 X. Zou, S. Xu, X. Chen, L. Yan and Y. Han, Breaking the von Neumann bottleneck: architecture-level processing-in-memory technology, *Sci. China Inf. Sci.*, 2021, **64**, 160404, DOI: 10.1007/s11432-020-3227-1.

23 L. Chen, J. Xi, E. K. Tekelenburg, K. Tran, G. Portale, C. J. Brabec and M. A. Loi, Quasi-2D Lead–Tin Perovskite Memory Devices Fabricated by Blade Coating, *Small Methods*, 2024, **8**, 2300040, DOI: 10.1002/smtd.202300040.

24 M. M. Ganaie, G. Bravetti, S. Sahu, M. Kumar and J. V. Milić, Resistive switching in benzylammonium-based Ruddlesden–Popper layered hybrid perovskites for non-volatile memory and neuromorphic computing, *Mater. Adv.*, 2024, **5**, 1880–1886, DOI: 10.1039/D3MA00618B.

25 M. Loizos, K. Rogdakis, W. Luo, P. Zimmermann, A. Hinderhofer, J. Lukić, M. Tountas, F. Schreiber, J. V. Milić and E. Kymakis, Resistive switching memories with enhanced durability enabled by mixed-dimensional perfluoroarene perovskite heterostructures, *Nanoscale Horiz.*, 2024, **9**, 1146–1154, DOI: 10.1039/D4NH00104D.

© 2026 The Author(s). Published by the Royal Society of Chemistry

Open Access Article. Published on 03 octobre 2025. Downloaded on 2026-02-04 10:39:24.
This article is licensed under a Creative Commons Attribution 3.0 Unported Licence.

26 D. Thrithamarassery Gangadharan and D. Ma, Searching for stability at lower dimensions: current trends and future prospects of layered perovskite solar cells, *Energy Environ. Sci.*, 2019, **12**, 2860–2889, DOI: 10.1039/C9EE01591D.
27 X. Dong, X. Li, X. Wang, Y. Zhao, W. Song, F. Wang, S. Xu, Z. Miao and Z. Wu, Improve the Charge Carrier Transporting in Two-Dimensional Ruddlesden–Popper Perovskite Solar Cells, *Adv. Mater.*, 2024, **36**, 2313056, DOI: 10.1002/adma.202313056.
28 L. Mao, C. C. Stoumpos and M. G. Kanatzidis, Two-Dimensional Hybrid Halide Perovskites: Principles and Promises, *J. Am. Chem. Soc.*, 2019, **141**, 1171–1190, DOI: 10.1021/jacs.8b10851.
29 X. Han, Y. Zheng, S. Chai, S. Chen and J. Xu, 2D organic-inorganic hybrid perovskite materials for nonlinear optics, *Nanophotonics*, 2020, **9**, 1787–1810, DOI: 10.1515/nanoph-2020-0038.
30 S. S. Khamgaonkar, A. Leudjo Taka and V. Maheshwari, Engineering and Design of Halide Perovskite Photoelectrochemical Cells for Solar-Driven Water Splitting, *Adv. Funct. Mater.*, 2024, **34**, 2405414, DOI: 10.1002/adfm.202405414.
31 K.-H. Wang, B.-S. Zhu, J.-S. Yao and H.-B. Yao, Chemical regulation of metal halide perovskite nanomaterials for efficient light-emitting diodes, *Sci. China: Chem.*, 2018, **61**, 1047–1061, DOI: 10.1007/s11426-018-9325-7.
32 A. H. Howlader, F. Li and R. Zheng, Carbon Nanomaterials for Halide Perovskites-Based Hybrid Photodetectors, *Adv. Mater. Technol.*, 2020, **5**, 2000643, DOI: 10.1002/admt.202000643.
33 J. Y. Park, Y. H. Lee, H. Kim and L. Dou, Two-dimensional perovskite heterostructures for single crystal semiconductor devices, *J. Appl. Phys.*, 2023, **134**, 060901, DOI: 10.1063/5.0153306.
34 H. Kim, D. Hyun, M. Hilal, Z. Cai and C. W. Moon, 2D and Quasi-2D Halide Perovskite-Based Resistive Switching Memory Systems, *Electronics*, 2024, **13**, 3572, DOI: 10.3390/electronics13173572.
35 H. Kim, K. A. Huynh, S. Y. Kim, Q. Van Le and H. W. Jang, 2D and Quasi-2D Halide Perovskites: Applications and Progress, *Phys. Status Solidi RRL*, 2020, **14**, 1900435, DOI: 10.1002/pssr.201900435.
36 H. Tsai, R. Asadpour, J.-C. Blancon, C. C. Stoumpos, J. Even, P. M. Ajayan, M. G. Kanatzidis, M. A. Alam, A. D. Mohite and W. Nie, Design principles for electronic charge transport in solution-processed vertically stacked 2D perovskite quantum wells, *Nat. Commun.*, 2018, **9**, 2130, DOI: 10.1038/s41467-018-04430-2.
37 S. Peng, J. Ma, P. Li, S. Zang, Y. Zhang and Y. Song, Regulation of Quantum Wells Width Distribution in 2D Perovskite Films for Photovoltaic Application, *Adv. Funct. Mater.*, 2022, **32**, 2205289, DOI: 10.1002/adfm.202205289.
38 X. Liu, X. Jiang, Y. Yin, J. Zhang, H. Tian, J. Guo, X. Guo and C. Li, Dominating (111) facets with ordered stacking in perovskite films, *Energy Environ. Sci.*, 2024, **17**, 6058–6067, DOI: 10.1039/D4EE01863J.
39 M. Javed, M. Benkraouda and N. Amrane, Theoretical investigation of octahedral tilting and bandgap non-linearity in monolayer Ruddlesden–Popper $A_2Pb_{1-x}Ge_xI_4$ perovskites, *Int. J. Energy Res.*, 2022, **46**, 18588–18608, DOI: 10.1002/er.8474.
40 M. Javed, A. Noureddine and M. Benkraouda, Band gap tailoring with octahedral distortion and bader charge analysis for 2D-Ruddlesden–Popper monolayer tin halide perovskites, *Mater. Sci. Semicond. Process.*, 2023, **162**, 107490, DOI: 10.1016/j.mssp.2023.107490.
41 G. Wei, A. B. Kaplan, H. Zhang, Y. Loo and M. A. Webb, Effects of Ligand Chemistry on Ion Transport in 2D Hybrid Organic–Inorganic Perovskites, *Adv. Energy Mater.*, 2024, **14**, 2401087, DOI: 10.1002/aenm.202401087.
42 G. Wu, R. Zhang, H. Wang, K. Ma, J. Xia, W. Lv, G. Xing and R. Chen, Rational Strategies to Improve the Efficiency of 2D Perovskite Solar Cells, *Adv. Mater.*, 2024, 2405470, DOI: 10.1002/adma.202405470.
43 M. P. Hautzinger, W. Mihalyi-Koch and S. Jin, A-Site Cation Chemistry in Halide Perovskites, *Chem. Mater.*, 2024, **36**, 10408–10420, DOI: 10.1021/acs.chemmater.4c02043.
44 G. J. Man, C. Kamal, A. Kalinko, D. Phuyal, J. Acharya, S. Mukherjee, P. K. Nayak, H. Rensmo, M. Odelius and S. M. Butorin, A-site cation influence on the conduction band of lead bromide perovskites, *Nat. Commun.*, 2022, **13**, 3839, DOI: 10.1038/s41467-022-31416-y.
45 D. Ghosh, A. R. Smith, A. B. Walker and M. S. Islam, Mixed A-Cation Perovskites for Solar Cells: Atomic-Scale Insights Into Structural Distortion, Hydrogen Bonding, and Electronic Properties, *Chem. Mater.*, 2018, **30**, 5194–5204, DOI: 10.1021/acs.chemmater.8b01851.
46 Q. Li, B. Xu and Z. Quan, Pressure-Regulated Excitonic Transitions in Emergent Metal Halides, *Acc. Chem. Res.*, 2023, **56**, 3282–3291, DOI: 10.1021/acs.accounts.3c00537.
47 D. Powell, K. R. Hansen, L. Flannery and L. Whittaker-Brooks, Traversing Excitonic and Ionic Landscapes: Reduced-Dimensionality-Inspired Design of Organometal Halide Semiconductors for Energy Applications, *Acc. Chem. Res.*, 2021, **54**, 4371–4382, DOI: 10.1021/acs.accounts.1c00492.
48 M. Gao, H. Liu, S. Yu, S. Louisia, Y. Zhang, D. P. Nenon, A. P. Alivisatos and P. Yang, Scaling Laws of Exciton Recombination Kinetics in Low Dimensional Halide Perovskite Nanostructures, *J. Am. Chem. Soc.*, 2020, **142**, 8871–8879, DOI: 10.1021/jacs.0c02000.
49 H. Baishya, R. Das Adhikari, M. J. Patel, D. Yadav, T. Sarmah, M. Alam, M. Kalita and P. K. Iyer, Defect mediated losses and degradation of perovskite solar cells: Origin, impacts and reliable characterization techniques, *J. Energy Chem.*, 2024, **94**, 217–253, DOI: 10.1016/j.jechem.2024.02.062.
50 B. Chen, S. Wang, Y. Song, C. Li and F. Hao, A critical review on the moisture stability of halide perovskite films and solar cells, *Chem. Eng. J.*, 2022, **430**, 132701, DOI: 10.1016/j.cej.2021.132701.
51 Y. Lei, Y. Xu, M. Wang, G. Zhu and Z. Jin, Origin, Influence, and Countermeasures of Defects in Perovskite Solar Cells, *Small*, 2021, **17**, 2005495, DOI: 10.1002/smll.202005495.

Open Access Article. Published on 03 octobre 2025. Downloaded on 2026-02-04 10:39:24. This article is licensed under a Creative Commons Attribution 3.0 Unported Licence.

52 N. K. Tailor, A. Mahapatra, A. Kalam, M. Pandey, P. Yadav and S. Satapathi, Influence of the A-site cation on hysteresis and ion migration in lead-free perovskite single crystals, *Phys. Rev. Mater.*, 2022, **6**, 045401, DOI: 10.1103/PhysRevMaterials.6.045401.

53 R. Kumar, P. Srivastava and M. Bag, Role of A-Site Cation and X-Site Halide Interactions in Mixed-Cation Mixed-Halide Perovskites for Determining Anomalously High Ideality Factor and the Super-linear Power Law in AC Ionic Conductivity at Operating Temperature, *ACS Appl. Electron. Mater.*, 2020, **2**, 4087–4098, DOI: 10.1021/acsaelm.0c00874.

54 P. Srivastava, R. Kumar and M. Bag, Discerning the Role of an A-Site Cation and X-Site Anion for Ion Conductivity Tuning in Hybrid Perovskites by Photoelectrochemical Impedance Spectroscopy, *J. Phys. Chem. C*, 2021, **125**, 211–222, DOI: 10.1021/acs.jpcc.0c09443.

55 Q. Gao, J. Qi, K. Chen, M. Xia, Y. Hu, A. Mei and H. Han, Halide Perovskite Crystallization Processes and Methods in Nanocrystals, Single Crystals, and Thin Films, *Adv. Mater.*, 2022, **34**, 2200720, DOI: 10.1002/adma.202200720.

56 J. Li, Z. Han, Y. Gu, D. Yu, J. Liu, D. Hu, X. Xu and H. Zeng, Perovskite Single Crystals: Synthesis, Optoelectronic Properties, and Application, *Adv. Funct. Mater.*, 2021, **31**, 2008684, DOI: 10.1002/adfm.202008684.

57 K. Zheng, K. Žídek, M. Abdellah, M. E. Messing, M. J. Al-Marri and T. Pullerits, Trap States and Their Dynamics in Organometal Halide Perovskite Nanoparticles and Bulk Crystals, *J. Phys. Chem. C*, 2016, **120**, 3077–3084, DOI: 10.1021/acs.jpcc.6b00612.

58 A. Mukherjee, M. Roy, N. Pathoor, M. Aslam and A. Chowdhury, Influence of Atmospheric Constituents on Spectral Instability and Defect-Mediated Carrier Recombination in Hybrid Perovskite Nanoplatelets, *J. Phys. Chem. C*, 2021, **125**, 17133–17143, DOI: 10.1021/acs.jpcc.1c02207.

59 M. García-Batlle, J. Mayén Guillén, M. Chapran, O. Baussens, J. Zaccaro, J.-M. Verilhac, E. Gros-Daillon, A. Guerrero, O. Almora and G. Garcia-Belmonte, Coupling between Ion Drift and Kinetics of Electronic Current Transients in $MAPbBr_3$ Single Crystals, *ACS Energy Lett.*, 2022, **7**, 946–951, DOI: 10.1021/acsenergylett.1c02578.

60 Y. Zhao, W. Zhou, Z. Han, D. Yu and Q. Zhao, Effects of ion migration and improvement strategies for the operational stability of perovskite solar cells, *Phys. Chem. Chem. Phys.*, 2021, **23**, 94–106, DOI: 10.1039/D0CP04418K.

61 N. Li, Y. Jia, Y. Guo and N. Zhao, Ion Migration in Perovskite Light-Emitting Diodes: Mechanism, Characterizations, and Material and Device Engineering, *Adv. Mater.*, 2022, **34**, 2108102, DOI: 10.1002/adma.202108102.

62 T. Zhang, C. Hu and S. Yang, Ion Migration: A ''Double-Edged Sword'' for Halide-Perovskite-Based Electronic Devices, *Small Methods*, 2020, **4**, 1900552, DOI: 10.1002/smtd.201900552.

63 H. Chen, Two-Step Sequential Deposition of Organometal Halide Perovskite for Photovoltaic Application, *Adv. Funct. Mater.*, 2017, **27**, 1605654, DOI: 10.1002/adfm.201605654.

64 M. R. Ahmadian-Yazdi, F. Zabihi, M. Habibi and M. Eslamian, Effects of Process Parameters on the Characteristics of Mixed-Halide Perovskite Solar Cells Fabricated by One-Step and Two-Step Sequential Coating, *Nanoscale Res. Lett.*, 2016, **11**, 408, DOI: 10.1186/s11671-016-1601-8.

65 A. Günzler, E. Bermúdez-Ureña, L. A. Muscarella, M. Ochoa, E. Ochoa-Martínez, B. Ehrler, M. Saliba and U. Steiner, Shaping Perovskites: *In Situ* Crystallization Mechanism of Rapid Thermally Annealed, Prepatterned Perovskite Films, *ACS Appl. Mater. Interfaces*, 2021, **13**, 6854–6863, DOI: 10.1021/acsami.0c20958.

66 C. Bi, Y. Shao, Y. Yuan, Z. Xiao, C. Wang, Y. Gao and J. Huang, Understanding the formation and evolution of interdiffusion grown organolead halide perovskite thin films by thermal annealing, *J. Mater. Chem. A*, 2014, **2**, 18508–18514, DOI: 10.1039/C4TA04007D.

67 D. Yang, W. Ming, H. Shi, L. Zhang and M.-H. Du, Fast Diffusion of Native Defects and Impurities in Perovskite Solar Cell Material $CH_3NH_3PbI_3$, *Chem. Mater.*, 2016, **28**, 4349–4357, DOI: 10.1021/acs.chemmater.6b01348.

68 J.-H. Yang, W.-J. Yin, J.-S. Park and S.-H. Wei, Fast self-diffusion of ions in $CH_3NH_3PbI_3$: the interstiticaly mechanism *versus* vacancy-assisted mechanism, *J. Mater. Chem. A*, 2016, **4**, 13105–13112, DOI: 10.1039/C6TA03599J.

69 H. Kim, J. S. Han, S. G. Kim, S. Y. Kim and H. W. Jang, Halide perovskites for resistive random-access memories, *J. Mater. Chem. C*, 2019, **7**, 5226–5234, DOI: 10.1039/C8TC06031B.

70 H. Kim, J. S. Han, J. Choi, S. Y. Kim and H. W. Jang, Halide Perovskites for Applications beyond Photovoltaics, *Small Methods*, 2018, **2**, 1700310, DOI: 10.1002/smtd.201700310.

71 J. S. Han, Q. Van Le, J. Choi, K. Hong, C. W. Moon, T. L. Kim, H. Kim, S. Y. Kim and H. W. Jang, Air-Stable Cesium Lead Iodide Perovskite for Ultra-Low Operating Voltage Resistive Switching, *Adv. Funct. Mater.*, 2018, **28**, 1705783, DOI: 10.1002/adfm.201705783.

72 H. Kim, M. Choi, J. M. Suh, Y.-S. Shim, I. H. Im, D. Hyun, S. J. Yang, Z. Cai, M. Hilal, M. G. Lee, C. W. Moon, S. Y. Kim and H. W. Jang, Resistive random-access memories using quasi-2D halide perovskites for wafer-scale reliable switching behaviors, *Mater. Sci. Semicond. Process.*, 2024, **182**, 108718, DOI: 10.1016/j.mssp.2024.108718.

73 J. S. Han, Q. Van Le, H. Kim, Y. J. Lee, D. E. Lee, I. H. Im, M. K. Lee, S. J. Kim, J. Kim, K. J. Kwak, M. Choi, S. A. Lee, K. Hong, S. Y. Kim and H. W. Jang, Lead-Free Dual-Phase Halide Perovskites for Preconditioned Conducting-Bridge Memory, *Small*, 2020, **16**, 2003225, DOI: 10.1002/smll.202003225.

74 H. Kim, J. S. Kim, J. Choi, Y.-H. Kim, J. M. Suh, M.-J. Choi, Y.-S. Shim, S. Y. Kim, T.-W. Lee and H. W. Jang, $MAPbBr_3$ Halide Perovskite-Based Resistive Random-Access Memories Using Electron Transport Layers for Long Endurance Cycles and Retention Time, *ACS Appl. Mater. Interfaces*, 2024, **16**, 2457–2466, DOI: 10.1021/acsami.3c01450.

75 J. S. Han, Q. Van Le, J. Choi, H. Kim, S. G. Kim, K. Hong, C. W. Moon, T. L. Kim, S. Y. Kim and H. W. Jang, Lead-Free

© 2026 The Author(s). Published by the Royal Society of Chemistry

Open Access Article. Published on 03 octobre 2025. Downloaded on 2026-02-04 10:39:24. This article is licensed under a Creative Commons Attribution 3.0 Unported Licence.

All-Inorganic Cesium Tin Iodide Perovskite for Filamentary and Interface-Type Resistive Switching toward Environment-Friendly and Temperature-Tolerant Nonvolatile Memories, *ACS Appl. Mater. Interfaces*, 2019, **11**, 8155–8163, DOI: 10.1021/acsami.8b15769.

76 W. Sohn, H. Kim, J. H. Lee, Y.-S. Shim, C. W. Moon and H. Kim, Advances in resistive switching memory: comprehensive insights into ECM mechanisms through TEM observations and analysis, *Mater. Adv.*, 2025, **6**, 4158–4173, DOI: 10.1039/D5MA00337G.

77 S. Lee, H. Kim, D. H. Kim, W. Bin Kim, J. M. Lee, J. Choi, H. Shin, G. S. Han, H. W. Jang and H. S. Jung, Tailored 2D/3D Halide Perovskite Heterointerface for Substantially Enhanced Endurance in Conducting Bridge Resistive Switching Memory, *ACS Appl. Mater. Interfaces*, 2020, **12**, 17039–17045, DOI: 10.1021/acsami.9b22918.

78 H. Kim, I. H. Im, D. Hyun, M. Hilal, Z. Cai, S. J. Yang, Y.-S. Shim and C. W. Moon, Stretchable resistive switching memory devices for wearable systems, *J. Korean Ceram. Soc.*, 2025, **62**, 397–411, DOI: 10.1007/s43207-025-00497-y.

79 H. Kim, Recent Progress in Resistive Switching Memory Devices Covering Metal Oxides, Polymers, Bioinspired Materials, and Halide Perovskites, *Electron. Mater. Lett.*, 2025, **21**, 487–503, DOI: 10.1007/s13391-025-00579-3.

80 H. Kim, M.-J. Choi, J. M. Suh, J. S. Han, S. G. Kim, Q. Van Le, S. Y. Kim and H. W. Jang, Quasi-2D halide perovskites for resistive switching devices with ON/OFF ratios above 109, *NPG Asia Mater.*, 2020, **12**, 21, DOI: 10.1038/s41427-020-0202-2.

81 S. G. Kim, J. S. Han, H. Kim, S. Y. Kim and H. W. Jang, Recent Advances in Memristive Materials for Artificial Synapses, *Adv. Mater. Technol.*, 2018, **3**, 1800457, DOI: 10.1002/admt.201800457.

82 S. G. Kim, Q. Van Le, J. S. Han, H. Kim, M. Choi, S. A. Lee, T. L. Kim, S. B. Kim, S. Y. Kim and H. W. Jang, Dual-Phase All-Inorganic Cesium Halide Perovskites for Conducting-Bridge Memory-Based Artificial Synapses, *Adv. Funct. Mater.*, 2019, **29**, 1906686, DOI: 10.1002/adfm.201906686.

83 V. A. Filippov, A. N. Bobylev, A. N. Busygin, A. D. Pisarev and S. Yu Udovichenko, A biomorphic neuron model and principles of designing a neural network with memristor synapses for a biomorphic neuroprocessor, *Neural Comput. Appl.*, 2020, **32**, 2471–2485, DOI: 10.1007/s00521-019-04383-7.

84 R. Yang, H. Huang and X. Guo, Memristive Synapses and Neurons for Bioinspired Computing, *Adv. Electron. Mater.*, 2019, **5**, 1900287, DOI: 10.1002/aelm.201900287.

85 X. Zhang, H. Gu and F. Wu, Memristor reduces conduction failure of action potentials along axon with Hopf bifurcation, *Eur. Phys. J.-Spec. Top.*, 2019, **228**, 2053–2063, DOI: 10.1140/epjst/e2019-900004-2.

86 M. A. Shakib, Z. Gao and C. Lamuta, Synaptic Properties of Geopolymer Memristors: Synaptic Plasticity, Spike-Rate-Dependent Plasticity, and Spike-Timing-Dependent Plasticity, *ACS Appl. Electron. Mater.*, 2023, **5**, 4875–4884, DOI: 10.1021/acsaelm.3c00654.

87 H. Tan, S. Majumdar, Q. Qin, J. Lahtinen and S. van Dijken, Mimicking Neurotransmitter Release and Long-Term Plasticity by Oxygen Vacancy Migration in a Tunnel Junction Memristor, *Adv. Intell. Syst.*, 2019, **1**, 1900036, DOI: 10.1002/aisy.201900036.

88 J. H. Baek, I. H. Im, E.-M. Hur, J. Park, J. Lim, S. Kim, K. Kang, S. Y. Kim, J. Y. Song and H. W. Jang, Artificial synaptic devices based on biomimetic electrochemistry: A review, *Mater. Res. Bull.*, 2024, **176**, 112803, DOI: 10.1016/j.materresbull.2024.112803.

89 H. Yu, H. Wei, J. Gong, H. Han, M. Ma, Y. Wang and W. Xu, Evolution of Bio-Inspired Artificial Synapses: Materials, Structures, and Mechanisms, *Small*, 2021, **17**, 2000041, DOI: 10.1002/smll.202000041.

90 M. Huang, M. Schwacke, M. Onen, J. del Alamo, J. Li and B. Yildiz, Electrochemical Ionic Synapses: Progress and Perspectives, *Adv. Mater.*, 2023, **35**, 2205169, DOI: 10.1002/adma.202205169.

91 Y. Guo, F. Wu, G. Dun, T. Cui, Y. Liu, X. Tan, Y. Qiao, M. Lanza, H. Tian, Y. Yang and T. Ren, Electrospun Nanofiber-Based Synaptic Transistor with Tunable Plasticity for Neuromorphic Computing, *Adv. Funct. Mater.*, 2023, **33**, 2208055, DOI: 10.1002/adfm.202208055.

92 M. Xu, X. Mai, J. Lin, W. Zhang, Y. Li, Y. He, H. Tong, X. Hou, P. Zhou and X. Miao, Recent Advances on Neuromorphic Devices Based on Chalcogenide Phase-Change Materials, *Adv. Funct. Mater.*, 2020, **30**, 2003419, DOI: 10.1002/adfm.202003419.

93 G. Vats, B. Hodges, A. J. Ferguson, L. M. Wheeler and J. L. Blackburn, Optical Memory, Switching, and Neuromorphic Functionality in Metal Halide Perovskite Materials and Devices, *Adv. Mater.*, 2023, **35**, 2205459, DOI: 10.1002/adma.202205459.

94 A. Khalid, A. M. Alanazi, S. A. Alderhami, A. H. Alsehli, M. M. Alsowayigh, A. M. Saeedi, H. B. Albargi and H. M. Al-Saidi, Impact of metallic and vacancy-oriented filamentary switching on memristor device based on $Cs_2AgInCl_6$ double halide perovskite, *Mater. Sci. Semicond. Process.*, 2023, **165**, 107678, DOI: 10.1016/j.mssp.2023.107678.

95 S. Chen and J. Huang, Recent Advances in Synaptic Devices Based on Halide Perovskite, *ACS Appl. Electron. Mater.*, 2020, **2**, 1815–1825, DOI: 10.1021/acsaelm.0c00180.

96 S. Kang, J. Shi, J. Feng, J. Fan, S. Xue, G. Cai and J. S. Zhao, Molecular Structure Engineering of Polyelectrolyte Bilayer-Based Memristors: Implications for Linear Potentiation and Depression Characteristics, *ACS Appl. Nano Mater.*, 2023, **6**, 3919–3926, DOI: 10.1021/acsanm.3c00005.

97 X. Li, Z. Fang, X. Guo, R. Wang, Y. Zhao, W. Zhu, L. Wang and L. Zhang, Light-Induced Conductance Potentiation and Depression in an All-Optically Controlled Memristor, *ACS Appl. Mater. Interfaces*, 2024, **16**, 27866–27874, DOI: 10.1021/acsami.4c02092.

98 D. Dong, W. Duan, X. Wang and H. Li, A Te-based memristor with short-term depression behavior, *J. Phys. D: Appl. Phys.*, 2025, **58**, 175101, DOI: 10.1088/1361-6463/adbf2d.

© 2026 The Author(s). Published by the Royal Society of Chemistry

Open Access Article. Published on 03 octobre 2025. Downloaded on 2026-02-04 10:39:24. This article is licensed under a Creative Commons Attribution 3.0 Unported Licence.

99 E. Miranda, G. Milano and C. Ricciardi, Modeling of Short-Term Synaptic Plasticity Effects in ZnO Nanowire-Based Memristors Using a Potentiation-Depression Rate Balance Equation, *IEEE Trans. Nanotechnol.*, 2020, **19**, 609–612, DOI: 10.1109/TNANO.2020.3009734.

100 R. Berdan, T. Prodromakis, A. Khiat, I. Salaoru, C. Toumazou, F. Perez-Diaz and E. Vasilaki, in 2013 IEEE International Symposium on Circuits and Systems (ISCAS2013), IEEE, 2013, pp. 425–428.

101 G. Antunes, A. C. Roque and F. M. Simoes-de-Souza, Stochastic Induction of Long-Term Potentiation and Long-Term Depression, *Sci. Rep.*, 2016, **6**, 30899, DOI: 10.1038/srep30899.

102 A. Kamal, G.-J. Biessels, I. J. A. Urban and W. H. Gispen, Hippocampal synaptic plasticity in streptozotocin-diabetic rats: impairment of long-term potentiation and facilitation of long-term depression, *Neuroscience*, 1999, **90**, 737–745, DOI: 10.1016/S0306-4522(98)00485-0.

103 A. Agrawal, C. Wang, T. Sharma and K. Roy, Magnetoresistive Circuits and Systems: Embedded Non-Volatile Memory to Crossbar Arrays, *IEEE Trans. Circuits Syst. I: Regul. Pap.*, 2021, **68**, 2281–2294, DOI: 10.1109/TCSI.2021.3069682.

104 Z. Chen, G. Zhang, H. Cai, C. Bengel, F. Liu, X. Zhao, S. Kvatinsky, H. Schmidt, R. Waser, S. Menzel and N. Du, Study on sneak path effect in self-rectifying crossbar arrays based on emerging memristive devices, *Front. Electron. Mater.*, 2022, **2**, 988785, DOI: 10.3389/femat.2022.988785.

105 S. H. Jo, T. Kumar, S. Narayanan and H. Nazarian, Cross-Point Resistive RAM Based on Field-Assisted Superlinear Threshold Selector, *IEEE Trans. Electron Devices*, 2015, **62**, 3477–3481, DOI: 10.1109/TED.2015.2426717.

106 A. Amirsoleimani, F. Alibart, V. Yon, J. Xu, M. R. Pazhouhandeh, S. Ecoffey, Y. Beilliard, R. Genov and D. Drouin, In-Memory Vector–Matrix Multiplication in Monolithic Complementary Metal–Oxide–Semiconductor-Memristor Integrated Circuits: Design Choices, Challenges, and Perspectives, *Adv. Intell. Syst.*, 2020, **2**, 2000115, DOI: 10.1002/aisy.202000115.

107 S. Kwon, T.-W. Kim, S. Jang, J.-H. Lee, N. D. Kim, Y. Ji, C.-H. Lee, J. M. Tour and G. Wang, Structurally Engineered Nanoporous Ta_2O_{5-x} Selector-Less Memristor for High Uniformity and Low Power Consumption, *ACS Appl. Mater. Interfaces*, 2017, **9**, 34015–34023, DOI: 10.1021/acsami.7b06918.

108 A. S. Sankpal and D. J. Pete, in 2020 4th International Conference on Electronics, Communication and Aerospace Technology (ICECA), IEEE, 2020, pp. 99–104.

109 P. A. Hoeher, M. Mewis and M. Liserre, Channel Coding and Receiver Design for Simultaneous Wireline Information and Power Transfer, *IEEE Open J. Power Electron.*, 2021, **2**, 545–558, DOI: 10.1109/OJPEL.2021.3117706.

110 S. Galli, A Novel Approach to the Statistical Modeling of Wireline Channels, *IEEE Trans. Commun.*, 2011, **59**, 1332–1345, DOI: 10.1109/TCOMM.2011.031611.090692.

111 T. Tanzawa, A. Umezawa, T. Taura, H. Shiga, T. Hara, Y. Takano, T. Miyaba, N. Tokiwa, K. Watanabe, H. Watanabe, K. Masuda, K. Naruke, H. Kato and S. Atsumi, A 44-mm/sup 2/four-bank eight-word page-read 64-Mb flash memory with flexible block redundancy and fast accurate word-line voltage controller, *IEEE J. Solid-State Circuits*, 2002, **37**, 1485–1492, DOI: 10.1109/JSSC.2002.802356.

112 J. Cai and C.-T. Sah, Gate tunneling currents in ultrathin oxide metal–oxide–silicon transistors, *J. Appl. Phys.*, 2001, **89**, 2272–2285, DOI: 10.1063/1.1337596.

113 M. Saravanan and E. Parthasarathy, A review of III-V Tunnel Field Effect Transistors for future ultra low power digital/analog applications, *Microelectron. J.*, 2021, **114**, 105102, DOI: 10.1016/j.mejo.2021.105102.

114 A. M. Ionescu and H. Riel, Tunnel field-effect transistors as energy-efficient electronic switches, *Nature*, 2011, **479**, 329–337, DOI: 10.1038/nature10679.

115 Y. Xi and B. Gao, Heterogeneous Integration and Co-design of Memristor and MOSFET for AI Application, *ECS Trans.*, 2020, **98**, 3–8, DOI: 10.1149/09805.0003ecst.

116 E. P.-B. Quesada, T. Rizzi, A. Gupta, M. K. Mahadevaiah, A. Schubert, S. Pechmann, R. Jia, M. Uhlmann, A. Hagelauer, C. Wenger and E. Perez, in 2023 14th Spanish Conference on Electron Devices (CDE), IEEE, 2023, pp. 1–4.

117 M. Sivan, Y. Li, H. Veluri, Y. Zhao, B. Tang, X. Wang, E. Zamburg, J. F. Leong, J. X. Niu, U. Chand and A. V.-Y. Thean, All WSe_2 1T1R resistive RAM cell for future monolithic 3D embedded memory integration, *Nat. Commun.*, 2019, **10**, 5201, DOI: 10.1038/s41467-019-13176-4.

118 L. Brackmann, T. Ziegler, A. Jafari, D. J. Wouters, M. B. Tahoori and S. Menzel, Improved Arithmetic Performance by Combining Stateful and Non-Stateful Logic in Resistive Random Access Memory 1T–1R Crossbars, *Adv. Intell. Syst.*, 2024, **6**, 2300579, DOI: 10.1002/aisy.202300579.

119 P. Thakkar, J. Gosai, H. J. Gogoi and A. Solanki, From fundamentals to frontiers: a review of memristor mechanisms, modeling and emerging applications, *J. Mater. Chem. C*, 2024, **12**, 1583–1608, DOI: 10.1039/D3TC03692H.

120 G. Zhang, J. Qin, Y. Zhang, G. Gong, Z. Xiong, X. Ma, Z. Lv, Y. Zhou and S. Han, Functional Materials for Memristor-Based Reservoir Computing: Dynamics and Applications, *Adv. Funct. Mater.*, 2023, **33**, 2302929, DOI: 10.1002/adfm.202302929.

121 Y. Zhao, Z. Lou, J. Hu, Z. Li, L. Xu, Z. Chen, Z. Xu, T. Wang, M. Wu, H. Ying, M. An, W. Li, X. Lin and X. Zheng, Scalable Layer-Controlled Oxidation of Bi_2O_2Se for Self-Rectifying Memristor Arrays With sub-pA Sneak Currents, *Adv. Mater.*, 2024, **36**, 2406608, DOI: 10.1002/adma.202406608.

122 T. D. Dongale, G. U. Kamble, D. Y. Kang, S. S. Kundale, H.-M. An and T. G. Kim, Recent Progress in Selector and Self-Rectifying Devices for Resistive Random-Access Memory Application, *Phys. Status Solidi RRL*, 2021, **15**, 2100199, DOI: 10.1002/pssr.202100199.

123 J. H. Yoon, D. E. Kwon, Y. Kim, Y. J. Kwon, K. J. Yoon, T. H. Park, X. L. Shao and C. S. Hwang, The current limit and self-rectification functionalities in the TiO_2/HfO_2 resistive switching material system, *Nanoscale*, 2017, **9**, 11920–11928, DOI: 10.1039/C7NR02215H.

© 2026 The Author(s). Published by the Royal Society of Chemistry

Open Access Article. Published on 03 octobre 2025. Downloaded on 2026-02-04 10:39:24.
This article is licensed under a Creative Commons Attribution 3.0 Unported Licence.

124 B. H. Calhoun, F. A. Honore and A. P. Chandrakasan, A leakage reduction methodology for distributed MTCMOS, *IEEE J. Solid-State Circuits*, 2004, **39**, 818–826, DOI: 10.1109/JSSC.2004.826335.

125 S. Zander, G. Armitage and P. Branch, A survey of covert channels and countermeasures in computer network protocols, *IEEE Commun. Surv. Tutor.*, 2007, **9**, 44–57, DOI: 10.1109/COMST.2007.4317620.

126 M. A. Zidan, H. A. H. Fahmy, M. M. Hussain and K. N. Salama, Memristor-based memory: The sneak paths problem and solutions, *Microelectron. J.*, 2013, **44**, 176–183, DOI: 10.1016/j.mejo.2012.10.001.

127 S. Y. Kim, J. M. Yang, S. H. Lee and N. G. Park, A layered $(n\text{-}C_4H_9NH_3)_2CsAgBiBr_7$ perovskite for bipolar resistive switching memory with a high ON/OFF ratio, *Nanoscale*, 2021, **13**, 12475–12483, DOI: 10.1039/d1nr03245c.

128 Y. Kim, S. J. Baik and H. Shin, Vertically oriented 2D layered perovskite-based resistive random access memory (ReRAM) crossbar arrays, *Curr. Appl. Phys.*, 2022, **44**, 46–54, DOI: 10.1016/j.cap.2022.09.003.

129 S. J. Kim, I. H. Im, J. H. Baek, S. H. Park, J. Y. Kim, J. J. Yang and H. W. Jang, Reliable and Robust Two-Dimensional Perovskite Memristors for Flexible-Resistive Random-Access Memory Array, *ACS Nano*, 2024, **18**, 28131–28141, DOI: 10.1021/acsnano.4c07673.

130 X. Chen, X. Pan, B. Jiang, J. Wei, Y. Long, J. Tang, X. Li, J. Zhang, J. Duan, L. Tao, G. Ma and H. Wang, Strongly stable resistive random access memory based on quasi-two-dimensional perovskites, *Sci. China Mater.*, 2024, **67**, 879–886, DOI: 10.1007/s40843-023-2738-5.

131 S. Kim, J. Yang, E. Choi and N. Park, Layered $(C_6H_5\text{-}CH_2NH_3)_2CuBr_4$ Perovskite for Multilevel Storage Resistive Switching Memory, *Adv. Funct. Mater.*, 2020, **30**, 2002653, DOI: 10.1002/adfm.202002653.

132 M. Kundar, K. Gayen, R. Ray, D. Kushavah and S. K. Pal, Highly stable two-dimensional Ruddlesden–Popper perovskite-based resistive switching memory devices, *Nanoscale*, 2024, **16**, 16159–16171, DOI: 10.1039/D4NR01395F.

133 J. Son, M. Lee, A. Sannyal, H. Yun, J. Cheon, S. Lee, J. S. Park, S. J. Kang, J. Jang and B. Jeong, Self-Rectifying Resistive Memory with a Ferroelectric and 2D Perovskite Lateral Heterostructure, *ACS Nano*, 2025, **19**, 10796–10806, DOI: 10.1021/acsnano.4c07869.

134 Y. Park and J.-S. Lee, Controlling the Grain Size of Dion–Jacobson-Phase Two-Dimensional Layered Perovskite for Memory Application, *ACS Appl. Mater. Interfaces*, 2022, **14**, 4371–4377, DOI: 10.1021/acsami.1c20272.

135 M. Khemnani, B. Tripathi, P. Thakkar, J. Gosai, M. Jain, P. Chandra and A. Solanki, Investigating the Role of Interfacial Layer for Resistive Switching in a Hybrid Dion-Jacobson Perovskite-Based Memristor, *ACS Appl. Electron. Mater.*, 2023, **5**, 5249–5256, DOI: 10.1021/acsaelm.3c01038.

136 S. Paramanik, A. Maiti, S. Chatterjee and A. J. Pal, Large Resistive Switching and Artificial Synaptic Behaviors in Layered $Cs_3Sb_2I_9$ Lead-Free Perovskite Memory Devices, *Adv. Electron. Mater.*, 2022, **8**, 2202118, DOI: 10.1002/aelm.202100237.

137 S. Ge, X. Guan, Y. Wang, C. Lin, Y. Cui, Y. Huang, X. Zhang, R. Zhang, X. Yang and T. Wu, Low-Dimensional Lead-Free Inorganic Perovskites for Resistive Switching with Ultralow Bias, *Adv. Funct. Mater.*, 2020, **30**, 2002110, DOI: 10.1002/adfm.202002110.

138 Y. Yuan, Y. Wang, W. Zhang, F. Qi, X. Tang and Z. Wang, Dimer-type $Cs_3Sb_2I_9$: An efficient perovskite material for low operating voltage and high stability flexible resistive switching memory, *J. Alloys Compd.*, 2023, **937**, 168308, DOI: 10.1016/j.jallcom.2022.168308.

139 S.-Y. Kim, D.-A. Park and N.-G. Park, Synthetic Powder-Based Thin (<0.1 μm) $Cs_3Bi_2Br_9$ Perovskite Films for Air-Stable and Viable Resistive Switching Memory, *ACS Appl. Electron. Mater.*, 2022, **4**, 2388–2395, DOI: 10.1021/acsaelm.2c00201.

140 U. Jung, D.-S. Woo, S. Kim, Z. Tan and J. Park, Anisotropic resistive switching of 2D-layered single crystal halide perovskite $CsPb_2Br_5$-based memristor, *Nano Res.*, 2025, **18**, 94907023, DOI: 10.26599/NR.2025.94907023.

© 2026 The Author(s). Published by the Royal Society of Chemistry